First-principles investigation on optoelectronic and mechanical properties of $\mathbf{CaZrO_{3-x}Se_x}$ $(x = 0, 1, 2, 3)$ perovskites

Student ID: MS211311
Session: 2021-2022

Thesis submitted to the Department of Physics at
Jashore University of Science and Technology
in partial fulfillment of the requirements
for the degree of Master of Science
in Physics

October 2024

Abstract

In this work, we investigate the structural, electronic, optical and mechanical properties of spin polarized $CaZrO_{3-x}Se_x$ $(x = 0, 1, 2, 3)$ perovskites using first-principles calculations based on density functional theory as implemented in the WIEN2k code. The crystal structure of the compounds $CaZrO_{3-x}Se_x$ $(x = 0, 1, 2, 3)$ changes from cubic phase of $CaZrO_3$ to tetragonal configuration for $CaZrO_2Se$ and $CaZrOSe_2$, eventually returning to a cubic phase in $CaZrSe_3$ with varying x values. The electronic structure reveals that $CaZrO_{3-x}Se_x$ $(x = 0, 1, 2, 3)$ compounds exhibit semiconducting behavior. However, as the parameter x increases from 0 to 3, the band gap value decreases from 3.44 eV to 0.23 eV. The elastic constants and mechanical properties such as Young modulus, shear modulus, and Poission ratio of $CaZrO_{3-x}Se_x$ $(x = 0, 1, 2, 3)$ materials have been obtained to show its mechanical stability and ductility where $CaZrO_2Se$ exhibits brittle characteristics. Additionally, the structural stabilities of these materials are ensured by the Goldschmidt's tolerance factor and negative forrmaion energy. Furtheremore, optical properties including the dielectric function, refractive index, absorption coefficient, optical conductivity, reflectivity, energy loss function and extinction coefficient are investigated in each case. In addition, good absorption coefficient, high optical conductivity and small reflectivity in the visible and ultraviolet region indicate that the $CaZrO_{3-x}Se_x$ $(x = 0, 1, 2, 3)$ perovskites have the potential to be used in diverse optoelectronic applications beyond photovoltaics.

Acknowledgements

Firstly, I praise and thank almighty Allah, the nourisher and the sustainer of the worlds and peace be upon the great prophet Muhammad and his companions. I am indebted to my supervisor Dr. Mohammad Abdur Rashid for his guidence, support and expertise throughout the entire process of this thesis. I would like to thank all the faculty members of the Department of Physics for their encouragements and insightful comments which driven me to prepare for my future career. To Salma Zahan, thank you for always lending an ear when I needed to talk through challenges and for providing thoughtful suggestions during our group discussions. Going through this journey together made it not only more manageable but also more fun. Also, my sincere appreciation goes to the Quantum Materials Simulation Lab (QMSL) for providing many resources such as books, computer, printer, and internet facilities throughout the course of my research. I am thankful to my lab mates for their sound advice, pep-talks, cups of tea and encouragement. Last but not the least, I would like to thanks my parents, brother and sisters for their constant support, love and motivation that encouraged me every step of the way.

Mst. Dil Afroj

Contents

List of Figures

List of Tables

First-principles investigation on optoelectronic and mechanical properties of $\mathbf{CaZrO_{3-x}Se_x}$ $(x = 0, 1, 2, 3)$ perovskites

Chapter 1

Introduction

Perovskite materials have gained significant interest of researchers over the past ten years due to their attractive material properties and potential applications in many industry and technological domain including electrode functionalities [1], water splitting [2], photovoltaic, spintronic, photocatalysis [3], and thermoelectric applications [4]. Recently, oxide perovskite compounds have received immense consideration due to their significant physical properties for optoelectronic devices [5–8]. On the other hand, chalcogenide perovskites have also been studied in recent years because they exhibit smaller band gaps than oxide perovskites and higher stability than halide perovskites. The invention of perovskite based solar cells have demonstrated remarkable advancements in converting solar power, with their efficiency rising from 3.8% in 2009 to an impressive 25.5% by 2020 [9]. Their sustained performance over time is impeded by susceptibility to environmental factors like moisture, light, and temperature, which can adversely affect their long-term stability [10, 11].

Within the fascinating perovskite oxides, $AZrO_3$ (A = Ca, Sr, Ba) are the most widely examined and most suitable for optoelectronic and thermoelectric properties. On the plane-wave ultrasoft pseudopotential technique based on the first-principles density functional theory (DFT), J. Liu et al. [12] investigated the structural, elastic, electronic and optical properties of the seven different phases of $SrZrO_3$ and they

obtained seven phases of $SrZrO_3$ are mechanically stable with cubic and tetragonal structures. When S.S.A. Gillani et al. investigated how magnesium doping influenced the band gap and optical characteristics of $SrZrO_3$ perovskite, they discovered that doping with magnesium changed the electronic band structure, making this material a desirable option for optoelectronic compounds [13]. To understand the electronic, optical and other characteristics of a perovskite material is essential to comprehend its usefulness in various fields. However, conducting experimental research requires a significant amount of resources and financial support. Density functional theory based computational investigations can point the way for experimental endeavours and, in many instances, provide a greater insight into the synthesized, associated features, and application of materials. Electronic, optical, elastic and many other property can be determined based on density functional theory accurately [14–18], and several observation shows its validity by comparing with experimental data.

In 2019 N.A. Noor et al. studied the pressure dependent optoelectronic and ground state thermoelectric properties of $MgZrO_3$ [19]. D.M. Hoatet al. investigated the configurational, electronic and photon related features of cubic perovskite $CaZrO_3$ and $CaHfO_3$ in 2018 [20]. The mechanical behavior of $CaZrO_3$ is also studied by Z.F. Hou in 2008 [21]. Among several cubic perovskites, $CaZrO_3$ has huge melting point, extremely low thermal extension, very high toughness, elevated chemical constancy and outstanding decay resistance in opposite to earth alkali oxides [22]. When M. Rashid et al. studied the pressure dependent physical characteristics of alkaline earth zirconates ($AZrO_3$; A = Ca, Ba, and Sr), they observed the band gap transition from indirect to direct when pressure is applied. They also realized that this agreement of the optical characteristics suggests practical optical applications [23]. The structural, electronic, and optical properties of pure $CaZrO_3$ perovskite have been tuned by the magnesium doping concentrations by fiest-principles computation based on DFT investigated theoretically by I. Zeba et al. and observed the electronic band gap decreases from 3.27 eV to 2.18 eV with increasing doping concentration. Analysis of optical properties with Mg doping reveals that the absorption edge of $CaZrO_3$ show the red shift and it would be very potential candidate for optoelec-

tronic application [24]. Yu-Liang Liu et al. [25] focused on tuning the photocatalytic performance of $NaTaO_3$ into the visible light range by doping S, Se, and Te elements. The decrease in band energy gaps and a significant enhancement of absorption coefficient in the visible light range is observed for the doped structure. The effects of sulfur, selenium, and tellurium on the electronic and optical properties of $LiNbO_3$ were studied by using density functional theory within WIEN2k code based on the generalized gradient approximation investigated by I. Ait Brahim et al. [26]. Chenhua Deng et al. [27] also observed transition metal-doped chalcogenide perovskite magnetic semiconductor for photovoltaic applications. The effects of three axial dilation strains and chalcogens-doped with dilation strain on electronic, optic, and thermoelectric properties of $BaSnO_3$ compound were examined by B. Akenoun et al. [28]. They found that the bandgap decreases while the increase of chalcogens elements in $BaSnO_3$ up to 5.0% and observed the absorption coefficient shifts into the visible region due to the reduction of bandgap which is quite recommended the photovoltaic applications.

M.A. Ali et al. [29] investigated the effect of S-substitution on the material's structure, electronic behavior, optical responses, mechanical strength, and thermodynamic characteristics of $KTaO_3$ and found that the band structure is affected by S doping and optical characteristics of S-doped $KTaO_3$ is a potentials maerial for opoelecronic application. Importantly, all these compounds have exhibited mechanical stability [29]. Moreover, the effect of dopants on the structural, electronic and optical properties of pristine $AgGaO_3$ and doped $Ag_{1-x}Cr_xGaO_3$ (x = 0.25, 0.50 and 0.75 at%) have been explored using first principle simulation by R.M. Arif Khalil et al. [30]. The physical properties of perovskites $CaZrO_{3-x}S_x$ ($x = 0, 1, 2, 3$) was investigated by H.Labrim et al.using DFT and observed the band gap changes from 3.36 eV to 0.48 eV with the change of x values. Along with they deduced that materials have good absorption coefficient which makes them suitable for optoelectronic applications [31].

Optroelectronic materials possess the remarkable ablity to initiate chemical reaction by hardnessing energy from absorbed light, which can be enhanced by replacing or

doping oxygen with chalcogenide atoms like sulfur (S) or selenium (Se) [32]. B. Mouhib et al. explored the electronic and optical properties on sulfur (S) and selenium (Se), or tellurium (Te) doping in $AZrO_3$-type perovskite compound through computational methods. These studies have observed a consistent trend: as the dopant concentration increases, the material's band gap decreases [33]. The electronic, optical and transport properties of perovskite $BaZrS_{3-x}Se_x$ compound doped with different concentrations of Se (x = 0%, 10%, 15% and 20%) are investigated by H. Zitouni et al. They found that the band gap values decreases by increasing the doping concentrations from 1.59 eV (for 0% of Se) to 1.35 eV (for 20% of Se). In addition to, $BaZrS_3$ perovskite have good optoelectronic properties for photovoltaic applications [34].

Therefore, we are motivated by the above work to investigate the optoelectronic and mechanical properties of $CaZrO_{3-x}Se_x$ $(x = 0, 1, 2, 3)$ perovskites to provide information on its potential applications in photovoltaic and optoelectronic devices. In this work, we start with the introduction of perovskite materials in the first chapter. In chapter 2 we discuss the basic quantum mechanics which starts with Schrödinger's equation as well as the theoretical investigation of density functional theory including the electron density, Thomas-Fermi theory, Hohenberg-Kohn theory, Kohn-Sham equations, solving the Khon-Sham equation, and the exchange-correlation potential such as local density approximation, generalized-gradient approximation. In Chapter 3, we present the outcomes with discussions of this thesis work. In this chapter, initially we focus on determining the crystal structure. Subsequently, we computed various properties, including electronic band structure, density of states, optical properties, as well as elastic properties of $CaZrO_{3-x}Se_x$ $(x = 0, 1, 2, 3)$. Finally, in chapter 4, we present our findings and show some possible applications of the studied compounds.

Chapter 2

Density Functional Theory

Computational approaches are becoming an integral part of the scientific world, particularly when calculating challenges. Computational and numerical methods are crucial for issues involving numerous amounts of particles, data, and so on that cannot be solved analytically. Furthermore, it requires a large amount of resources or financial support for the experiment. DFT is a type of ab initio method that is often referred to as a computational quantum mechanical modeling method. The method is well-known at the matter of quantum chemistry, condensed matter physics, materials science. The application of this method starts with remedying the many-body Schrödinger equation problem. However, DFT is more than just another method to solve the Schrödinger equation. DFT provides an entirely distinct approach to any interacting problem, translating it perfectly to more simple non-interacting problem. This methodology is broadly utilized for resolving a variety of issues, with the electronic structure problem being the most common [35]. In DFT, the electron density is used as the fundamental factor, instead of the wave-function. Another method for solving the many-body Schrödinger equation is the Hartree-Fock approach, that uses wave-functions to describe the electronic figure of atoms and substance. However, this methods has several drawbacks, including a high cost of calculation time for investigating big systems. But DFT has demonstrated superior accuracy at a re-

duced computing cost, making it superior to all other approaches. This facts makes DFT the most useful method to analyze electronic structure. Walter Kohn with his co-workers developed this "Density functional theory" and find out the way of using the electron density to resolve the Schrödinger equation. He got novel prize for his timeworn work [36]. The chapter provides an overview of fundamental quantum physics, its difficulties, and how DFT resolves them.

2.1 Schrödinger Equation

The Schrödinger equation is a fundamental equation in quantum mechanics that describes how the quantum state of a physical system changes. It is crucial for understanding the behaviour of particles at the atomic and sub-atomic levels such as electrons, photons and other quantum objects. It is a mathematical equation that was thought of by Erwin Schrödinger in 1925 [37]. The mathematical representation of Schrödinger equation is

$$\hat{H}\Psi = E\Psi, \tag{2.1}$$

where, $\hat{H}$ is the Hamiltonian operator, Ψ is the wave function of the system, and E is the energy eigenvalue representing the total energy of the quantum state. This equation is crucial in finding the stationary states of quantum systems. The Hamiltonian $\hat{H}$ represents the total energy operator of the system and is typically composed of two parts:

$$\hat{H} = \hat{T} + \hat{V}, \tag{2.2}$$

where, $\hat{T} = -\frac{\hbar^2}{2m}\nabla^2$ is the kinetic energy operator and $\hat{V} = V(\mathbf{r})$ is the potential energy operator. Putting this into the equation (2.1), the Schrödinger equation in three dimensions becomes

$$\left[-\frac{\hbar^2}{2m}\nabla^2 + V(\mathbf{r}) \right] \Psi(\mathbf{r}) = E\Psi(\mathbf{r}). \tag{2.3}$$

In one dimension, it simplifies to

$$\left[-\frac{\hbar^2}{2m}\frac{d^2\Psi(x)}{dx^2} + V(x)\Psi(x) \right] = E\Psi(x). \tag{2.4}$$

where, Ψ is a quantity associated with a moving particle. It is a complex quantity. The wave function Ψ has no physical meaning. The wave function Ψ describes the position of a particle with respect to time. It can be considered as probability amplitude. $\mid \Psi \mid^2$ is proportional to the probability of finding a particle at a particular time that is called probability density.

$$\mid \Psi \mid^2 = \mid \Psi^* \Psi \mid^2 \tag{2.5}$$

The wave function Ψ must be finite everywhere. If Ψ is finite for a particular point, it means an infinite large probability of finding the particles at that point. This would violates the uncertainity principles. It must be single valued. If Ψ has more than one value at any point, it means more than one value of probability of finding the particle at that point which is ridiculous. The wave function must be continuous and have a continuous first derivative everywhere and its must be normalizable.

For the sake of simplicity, the discussion is restricted to the time-independent wave function. A question always arising with physical quantities is about possible interpretations as well as observations. The Born probability interpretation of the wave function, which is a major principle of the Copenhagen interpretation of quantum mechanics, provides a physical interpretation for the square of the wave function as a probability density [36, 38]

$$P = |\psi(\mathbf{r}_1, \mathbf{r}_2, ...\mathbf{r}_N)|^2 d\mathbf{r}_1 d\mathbf{r}_2 .....d\mathbf{r}_N \tag{2.6}$$

Equation (2.6) describes the probability that particles 1,2,...,N are located simultaneously in the corresponding volume element $d\mathbf{r}_1 d\mathbf{r}_2 ... d\mathbf{r}_N$ [39]. What happens if the positions of two particles are exchanged, must be considered as well. Following merely logical reasoning, the overall probability density cannot depend on such an exchange,

$$|\Psi(\mathbf{r}_1, \mathbf{r}_2, ..., \mathbf{r}_i, \mathbf{r}_j, ..., \ \mathbf{r}_N)|^2 = |\Psi(\mathbf{r}_1, \mathbf{r}_2, ..., \mathbf{r}_j, \mathbf{r}_i, ..., \ \mathbf{r}_N)|^2 \tag{2.7}$$

There are only two possibilities for the behavior of the wave function during a

particle exchange. The first one is a symmetrical wave function, which does not change due to such an exchange. This corresponds to bosons (particles with integer or zero spin). The other possibility is an anti-symmetrical wave function, where an exchange of two particles causes a sign change, which corresponds to fermions (particles which half-integer spin) [40, 41].

In this text only electrons are from interest, which are fermions. The anti symmetric fermion wave function leads to the Pauli principle, which states that no two electrons can occupy the same state, whereas state means the orbital and spin parts of the wave function [42]. If equation (2.6) describes the probability of finding a particle in a volume element, setting the full range of coordinates as volume element must result in a probability of one, i.e. all particles must be found somewhere in space. This corresponds to the normalization condition for the wave function.

$$\int d\mathbf{r}_1 \int d\mathbf{r}_2 ... \int d\mathbf{r}_N |\psi(\mathbf{r}_1, \mathbf{r}_2, ...\mathbf{r}_N)|^2 = 1 \tag{2.8}$$

Equation (2.8) also gives insight on the requirements a wave function must fulfill in order to be physical acceptable. Wave functions must be continuous over the full spatial range and square-integratable [43]. The eigenfunctions Ψ_k with corresponding energy eigenvalues are E_k. The set Ψ_k is complete and Ψ_k may always be taken to be orthonormal and normalized

$$\int \Psi_k^* \Psi_l dx^N = \langle \Psi_k | \Psi_l \rangle = \delta_{kl} \tag{2.9}$$

We denote the ground state wave function and energy by Ψ_0 and E_0. Here, $\int dx_N$ means integration over 3N spatial coordinates and summation over N spin coordinates. Expectation values of observables are given by formula,

$$\langle \hat{A} \rangle = \frac{\int \Psi^* A \Psi dx}{\int \Psi^* \Psi dx} \tag{2.10}$$

where, $\hat{A}$ is the Hermitian linear operator for the observable A. If Ψ is normalized,

expectation values of kinetic and potential energy are given by the formulas

$$T[\Psi] = \langle \hat{T} \rangle = \int \Psi^* T \Psi dx \tag{2.11}$$

$$V[\Psi] = \langle \hat{V} \rangle = \int \Psi^* V \Psi dx \tag{2.12}$$

When a system is in the state Ψ, which may or may not satisfy equation (2.1), the average of many measurements of the energy is given by the formula

$$E[\Psi] = \frac{\langle \Psi | \hat{H} | \Psi \rangle}{\langle \Psi \rangle} \tag{2.13}$$

where,

$$\langle \Psi | \hat{H} | \Psi \rangle = \int \Psi^* \hat{H} \Psi dx \tag{2.14}$$

Since furthermore, each particular measurement of the energy gives one of the eigenvalues of $\hat{H}$, we immediately have

$$E[\Psi] \geq E_0 \tag{2.15}$$

The energy computed from a guessed Ψ is an upper bound to the true ground state energy E_0. Full minimization of the functional $E[\Psi]$ with respect to all allowed N-electron wave functions will give the true ground state Ψ_0 and energy $E[\Psi_0] = E_0$, that is,

$$E_0 = \min_{\Psi} E[\Psi] \tag{2.16}$$

Formal proof of minimum energy principle goes on follows. Expanding Ψ in terms of normalized eigenstates of $\hat{H}$

$$\Psi = \sum_k C_k \Psi_k \tag{2.17}$$

Then the energy becomes,

$$E[\Psi] = \frac{\sum_k |C_k|^2 E_k}{\sum_k |C_k|^2} \tag{2.18}$$

where E_k is the energy k^{th} eigenstate of $\hat{H}$. Noting that, the orthogonality of the Ψ_k

has been used. Because $E_0 \leq E_1 \leq ... \leq E_N$. $E(\Psi)$ is always greater than or equal to E_0 and it reaches its minimum if and only if $\Psi = C_0\Psi_0$. Every eigenstate Ψ is an extremum of the function $E[\Psi]$. In other words one may replace the Schrödinger equation with the variational principle

$$\delta E[\Psi] = 0 \tag{2.19}$$

2.2 Born-Oppenheimer (BO) Approximation

The Born-Oppenheimer approximation is a fundamental concept in quantum mechanics, particularly in the context of molecular and condensed matter physics. It addresses the challenge of the many-body problem by making a crucial simplifying assumption. In condensed matter physics, the many-body problem arises because materials are composed of a large number of interacting particles (such as electrons and nuclei). The interactions between these particles are typically complex and can be described by quantum mechanical principles. The Hamiltonian of a many-body system consisting of nuclei and electrons can be written as [44],

$$\begin{aligned}\hat{H} = -\sum_I \frac{\hbar^2}{2M_I}\nabla^2_{\mathbf{R}_I} - \sum_i \frac{\hbar^2}{2m_e}\nabla^2_{\mathbf{r}_i} + \frac{1}{2}\sum_{I,J}\frac{Z_I Z_J e^2}{|\mathbf{R}_I - \mathbf{R}_J|} \\ + \frac{1}{2}\sum_{i,j}\frac{e^2}{|\mathbf{r}_i - \mathbf{r}_j|} - \sum_{I,i}\frac{Z_I e^2}{|\mathbf{R}_I - \mathbf{r}_i|}\end{aligned} \tag{2.20}$$

where, the indexes I, J run on nuclei, i and j on electrons, $\mathbf{R}_I$ and M_I are position and mass of the nuclei, $\mathbf{r}_i$ and m_e are position and mass of the electrons. $|\mathbf{R}_I - \mathbf{R}_J|$, $|\mathbf{R}_I - \mathbf{r}_i|$ and $|\mathbf{r}_i - \mathbf{r}_j|$ represent the distance between the nucleus-nucleus, nucleus-electron, and electron-electron. In the right hand side, first term $-\sum_I \frac{\hbar^2}{2M_I}\nabla^2_{\mathbf{R}_I}$ represents the kinetic energy of the nuclei. Second term $-\sum_i \frac{\hbar^2}{2m_e}\nabla^2_{\mathbf{r}_i}$ denotes the kinetic energy of electrons. Third term $\frac{1}{2}\sum_{I,J}\frac{Z_I Z_J e^2}{|\mathbf{R}_I - \mathbf{R}_J|}$ is for the potential energy of nuclei-nuclei interaction. Fourth term $\frac{1}{2}\sum_{i,j}\frac{e^2}{|\mathbf{r}_i - \mathbf{r}_j|}$ is for the potential energy of electron-electron coulomb interaction and the last term $\sum_{I,i}\frac{Z_I e^2}{|\mathbf{R}_I - \mathbf{r}_i|}$ represents the potential energy of nuclei-electron coulomb interaction.

In condensed matter physics, Born-Oppenheimer (BO) approximation is the well known mathematical approximation. Specifically, it is the assumption that the wave function of atomic nuclei and electrons in a molecule can be treated separately, based on the fact that the nuclei are much heavier than electrons [45]. Due to larger relative mass of a nucleus compared to an electron, the coordinates of the electrons are dynamic. The approach is named after Max Born and J. Robert Oppenheimer in 1927. This approximation is widely used in quantum mechanics to speed up the computation of molecular wavefunctions and other properties for large molecules. There are cases where the assumption of separable motion no longer holds, which make the approximation lose validity, but even then the approximation is usually used as a starting point for more refined methods. Applying Born-Oppenheimer approximation, the electronic Hamiltonian is grouped into three terms

$$\hat{H}_{elec} = -\sum_i \frac{\hbar^2}{2m_e}\nabla^2_{\mathbf{r}_i} + \frac{1}{2}\sum_{i,j}\frac{e^2}{|\mathbf{r}_i - \mathbf{r}_j|} - \sum_{I,i}\frac{Z_I e^2}{|\mathbf{R}_I - \mathbf{r}_i|}, \tag{2.21}$$

and the Schrödinger equation for a many-body system reduces to

$$\hat{H}_{elec}\Psi = -\sum_i \frac{\hbar^2}{2m_e}\nabla^2_{\mathbf{r}_i}\Psi + \frac{1}{2}\sum_{i,j}\frac{e^2}{|\mathbf{r}_i - \mathbf{r}_j|}\Psi - \sum_{I,i}\frac{Z_I e^2}{|\mathbf{R}_I - \mathbf{r}_i|}\Psi. \tag{2.22}$$

As soon as the potential is known, the next step is the determination of the wave function, which contains all information about the system. As simple as that sounds, the exact knowledge of the potential is not possible for most natural systems, i.e. in similarity to classical mechanics, the largest system which can be solved analytically is a two-body system, which corresponding to a hydrogen atom. Using all approximations introduced up to now it is possible to calculate a problem similar to H_2^+, a single ionized hydrogen molecule. To get results for larger systems, further approximations have to be made.

2.3 The Hartree-Fock (HF) Approximation

If we can solve the electronic Schrödinger equation, we can describe the motion of the nuclei by introducing a nuclear Hamiltonian under the same assumptions used

to derive the electronic Schrödinger equation. So the major problem in condensed matter physics is to solve the electronic Schrödinger equation, which is the goal of the Hartree-Fock (HF) method. The Hartree-Fock approach is the first standard approach to many body system which was applied in 1930 by Fock [46]. The problems which are not possible to solve analitycallay of many body problems, this approach gives a suitable strategy to approximate it. It is as similar as the Least Action Principle of classical mechanics. For now, we have the interest only on the electronic Schrödinger equation. Therefore, we get $\hat{H} \equiv \hat{H}_{elec}$, $\hat{E} \equiv \hat{E}_{elec}$. The energy as observable corresponds to the general Hamiltonian operator can be calculated as [47, 48],

$$E = \langle \hat{H} \rangle = \int d\mathbf{r}_1 \int d\mathbf{r}_2 ... \int d\mathbf{r}_N \Psi^*(\mathbf{r}_1, \mathbf{r}_2, ..., \mathbf{r}_N) \hat{H} \Psi(\mathbf{r}_1, \mathbf{r}_2, ..., \mathbf{r}_N) \tag{2.23}$$

If we take a wave function as a trial, the obtained energy is not the same as the actual ground state wave function. Actual ground state energy is always lower than the obtained energy. If trial wave function is equal as the ground state wave function, the energies in both cases are equal.

$$E_{trial} \geq E_0 \tag{2.24}$$

with

$$E_{trial} = \int d\mathbf{r}_1 \int d\mathbf{r}_2 ... \int d\mathbf{r}_N \Psi^*_{trial}(\mathbf{r}_1, \mathbf{r}_2, ..., \mathbf{r}_N) \hat{H} \Psi_{trial}(\mathbf{r}_1, \mathbf{r}_2, ..., \mathbf{r}_N) \tag{2.25}$$

and

$$E_0 = \int d\mathbf{r}_1 \int d\mathbf{r}_2 ... \int d\mathbf{r}_N \Psi^*_0(\mathbf{r}_1, \mathbf{r}_2, ..., \mathbf{r}_N) \hat{H} \Psi_0(\mathbf{r}_1, \mathbf{r}_2, ..., \mathbf{r}_N) \tag{2.26}$$

The expressions above are usually inconvenient to handle. For the sake of a compact notation, the following the Dirac's bra-ket notation can be applied to the above equation as [49],

$$\langle \Psi_{trial} | \hat{H} | \Psi_{trial} \rangle = E_{trial} \geq E_0 = \langle \Psi_0 | \hat{H} | \Psi_0 \rangle \tag{2.27}$$

Proof: The eigenfunctions ψ_i of the Hamiltonian $\hat{H}$ (each corresponding to an energy eigenvalue E_i) form a complete basis set, therefore any normalized trial wave function Ψ_{trial} can be linear combination of those eigenfunctions [50].

$$\Psi_{trial} = \sum_i \lambda_i \psi_i \tag{2.28}$$

The assumption is made that the eigenfunctions are orthogonal and normalized. Therefore, it follows that

$$\langle \Psi_{trial} | \hat{H} | \Psi_{trial} \rangle = 1 = \langle \sum_i \lambda_i \psi_i | \sum_j \lambda_j \psi_j \rangle = \sum_i \sum_j \lambda_i^* \lambda_j \langle \psi_i | \psi_j \rangle = \sum_j |\lambda_j|^2 \tag{2.29}$$

On the other hand, following equation (2.29)

$$E_{trial} = \langle \Psi_{trial} | \hat{H} | \Psi_{trial} \rangle = \langle \sum_i \lambda_i \psi_i | \hat{H} | \sum_j \lambda_j \psi_j \rangle = \sum_j E_j |\lambda_j|^2 \tag{2.30}$$

Together with the fact that the ground state energy E_0 is defined by the lowest possible energy, and therefore has the smallest eigenvalue ($E_0 \leq E_i$), it is found that

$$E_{trial} = \sum_j E_j |\lambda_j|^2 \geq E_0 \sum_j |\lambda_j|^2 \tag{2.31}$$

One of the key ideas of density functional theory is the mathematical framework mentioned above, which consists of rules that assign numerical values to functions. In constrant to functional, which takes a function as an input and produces numerical outputs, whereas a function receives a numerical input and produces a numerical output [51]. Expressed in terms of functional calculus, where $\Psi \longrightarrow N$ addresses all allowed N electron wave functions [52], this means

$$E_0 = \min_{\Psi \to N} E[\Psi] = \min_{\Psi \to N} \langle \Psi | \hat{H} | \Psi \rangle = \min_{\Psi \to N} \langle \Psi | \hat{T} + \hat{V} + \hat{U} | \Psi \rangle. \tag{2.32}$$

Due to the abundance of potential wave functions and, on the other hand, the constrained processing capacity and time, the solution for the N electron systems is almost unachievable. As in the restricted Hartree-Fock approximation, it is possible

to limit the search to a more manageable subset of wavefunctions. The search is restricted to the antisymmetric product of N one electron wave functions that approximates N wave functions. A wave function of this type is called Slater-determinant [53].

$$\Psi_0 \approx \phi_{SD} = (N!)^{-\frac{1}{2}} \begin{vmatrix} \chi_1(x_1) & \chi_2(x_1) & \cdots \chi_N(x_1) \\ \chi_1(x_2) & \chi_2(x_2) & \cdots \chi_N(x_2) \\ \vdots & \vdots & \vdots \\ \chi_1(x_N) & \chi_2(x_N) & \cdots \chi_N(x_N) \end{vmatrix} \tag{2.33}$$

It is important to note that the spin-orbitals $\chi_i(x_i)$ are depend on spatial coordinates as well as spin coordinates. Spin coordinates are introduced by the spin function, $x_i = \mathbf{r}_i, s$. The text by Szabo [42] and Holthausen [52] omits a through description of the spin orbitals and their properties. Returning to the variational principle and equation, the ground state energy approximated by a single slater determinan becomes

$$E_0 = \min_{\phi_{SD} \to N} E[\phi_{SD}] = \min_{\phi_{SD} \to N} \langle \phi_{SD} | \hat{H} | \phi_{SD} \rangle = \min_{\phi_{SD} \to N} \langle \phi_{SD} | \hat{T} + \hat{V} + \hat{U} | \phi_{SD} \rangle \tag{2.34}$$

A general expression for the Hartree-Fock Energy is obtained by uses of the slater determinant as a trial function. According to equation (2.29), the normalization integral $\langle \Psi_{HF} | \Psi_{HF} \rangle$ is equal to 1 and the energy expectation value is found to be given by the formula

$$E_{HF} = \langle \phi_{SD} | \hat{H} | \phi_{SD} \rangle = \sum_{i=1}^{N} H_i + \frac{1}{2} \sum_{i,j=1}^{N} (J_{ij} - K_{ij}) \tag{2.35}$$

where

$$H_i = \int \psi_i^*(x) [-\frac{1}{2} \nabla^2 + U(x)] \psi_i(x) dx \tag{2.36}$$

$$J_{i,j} = \int \int \psi_i(x_1) \psi_i^*(x_1) \frac{1}{r_{12}} \psi_j^*(x_2) \psi_j(x_2) dx_1 dx_2 \tag{2.37}$$

$$K_{i,j} = \int \int \psi_i(x_1) \psi_j(x_1) \frac{1}{r_{12}} \psi_i(x_2) \psi_j^*(x_2) dx_1 dx_2 \tag{2.38}$$

These integrals are all real and $J_{ij} \geq K_{ij} \geq 0$. J_{ij} are called Coulomb integrals and

K_{ij} are exchange integrals [42, 52]. We have the important equation

$$J_{ij} = K_{ii} \tag{2.39}$$

This is the reason the double summation in the equation that include $i = j$ terms. Minimization of equation subject to the orthonormalization conditions,

$$\psi_i^*(x)\psi_j(x)dx = \delta_{ij} \tag{2.40}$$

gives the Hartree-Fock differential equation

$$\hat{F}\Psi_i(x) = \sum_{j=1}^{N} \varepsilon_{ij}\psi_j(x) \tag{2.41}$$

Where,

$$\hat{F} = -\frac{1}{2}\nabla^2 + \mathbf{v} + \mathbf{g} \tag{2.42}$$

in which the Coulomb exchange operator $g(x_1)$ is given by

$$\mathbf{g} = \hat{j} - \hat{k} \tag{2.43}$$

Here,

$$J(x_1)f(x_1) = \sum_{k=1}^{N} \int \psi_k^*(x_2)\psi_k(x_2)\frac{1}{r_{12}}f(x_1)dx_2 \tag{2.44}$$

$$K(x_1)f(x_1) = \sum_{k=1}^{N} \int \psi_k^*(x_2)\psi_k(x_2)\frac{1}{r_{12}}\psi_k(x_1)dx_2 \tag{2.45}$$

with $f(x_1)$ an arbitrary function. The matrix ε consists of lagrange multipliers. Also,

$$\varepsilon_{ji}^* = \varepsilon_{ij} \tag{2.46}$$

where, ε is Hermitian. Now multiplying equation (2.35) with Ψ_i^* and integrating, one obtains the formula for orbital energies

$$\varepsilon \equiv \varepsilon_{ii} = \langle\psi_i|\hat{F}|\psi_i\rangle = H_i + \sum_{j=1}^{N}(J_{ij} - K_{ij}) \tag{2.47}$$

Summing over i and compearing with equation (2.38) we get,

$$E_{HF} = \sum_{i=1}^{N} \varepsilon_i - \hat{V}_{ee} \tag{2.48}$$

Where the symbol V_{ee} stands for electron electron repulsion energy.

$$\hat{V}_{ee} = \int \psi^*_{HF}(x^N)(\sum_{i<j} \frac{1}{r_{ij}})\psi_H(x^N)dx^N \frac{1}{2} \sum_{i,j=1}^{N} (J_{ij} - K_{ij}) \tag{2.49}$$

For the total molecular energy including nucleus-nucleus repulsion one has,

$$W_{HF} = \sum_{i=j}^{N} \varepsilon_i - \hat{V}_{ee} + \hat{V}_{nn} \tag{2.50}$$

Neither E_{HF} nor W_{HF} is equal to the sum of orbital energies. Hartree-Fock method is a non-linear self-consistent field.

2.4 Limitation and Failings of the Hartree-Fock (HF) Approximation

Atoms as well as molecules can have an even or odd number of electrons. If the number of electrons is even and all of them are located in double occupied spatial orbitals, the compound is in a singlet state. Such systems are called closed-shell systems. Compounds with an odd number of electrons as well as compounds with single occupied orbitals, i.e. species with triplet or higher ground state, are called open-shell systems respectively. These two types of systems correspond to two different approaches of the Hartree-Fock method. In the restricted HF-method (RHF), all electrons are considered to be paired in orbitals whereas in the unrestricted HF (UHF)-method this limitation is lifted totally. It is also possible to describe open-shell systems with a RHF approach where only the single occupied orbitals are excluded which is then called a restricted open-shell HF (ROHF) which is an approach closer to reality but also more complex and therefore less popular than UHF [52].

There are also closed-shell systems which require the unrestricted approach in order to get proper results. For instance, the description of the dissociation of H_2 (i.e. the behavior at large internuclear distance), where one electron must be located at one hydrogen atom, can logically not be obtained by the use of a system which places both electrons in the same spatial orbital. Therefore the choice of method is always a very important point in HF calculations. Kohn states several $M = p^5$ with $3 \leq p \leq 10$ parameters for an output with adequate accuracy in the investigations of the H_2 system [54]. For a system with $N = 100$ electrons, the number of parameters rises to,

$$M = p^{3N} = 3^{300} \rightarrow 10^{300} \approx 10^{150} \rightarrow 10^{300} \tag{2.51}$$

According to the equation (2.51), energy reduction would have to be done in a space with at least 10^{150} dimension, which is well above current computer capabilities. As a result, HF methods are limited to situations involving a modest number of electron ($N \approx 10$). This barrier commonly referred to as the exponential wall because of the exponential component in equation (2.49). Since a many electron wave function cannot be described entirely by a single Slater determinant, the energy obtained by HF calculations is always larger than the exact ground state energy. The most accurate energy obtainable by HF-methods is called the Hartree-Fock-limit. The Hartree-Fock-limit is the most precise energy that can be calculated using HF-methods. Since a many electron wave function cannot be described entirely by a single Slater determinant, the energy obtained by HF calculations is always larger than the exact ground state energy. The most accurate energy obtainable by HF-methods is called the Hartree-Fock-limit.

2.5 Correlation Energy

No single determinant or straightforward combination of a few determinants can ever accurately describe the wave function for a system with many interacting electrons. The calculation of the energy error, however, is here characterized as being negative. The difference between E_{HF} and E_{exact} is called correlation energy and

can be denoted as [55],

$$E_{corr}^{HF} = E_{min} - E_{HF}. \tag{2.52}$$

When atomic and molecular changes preserve the number and type of chemical bonds, correlation energy tends to remain constant, but it can fluctuate significantly and become decisive when bonds change. Its magnitude can range from a few hundredth of an atomic unit to hundreds of kilocalories per mole. Exchange energies are an order magnitude or bigger, even if the self exchange term is omitted. Despite the fact that E_{corr} is usually small against E_{min}, as in the example of a N_2 molecule where

$$E_{corr}^{HF} = 14.9eV < 0.001E_{min}. \tag{2.53}$$

It can have a huge influence. For instance, the experimental dissociation energy of the N_2 molecule is

$$E_{diss} = 9.9eV < E_{corr} \tag{2.54}$$

which corresponds to a large contribution of the correlation energy to relative energies such as reaction energies which are of particular interest in quantum chemistry. The main contribution to the correlation energy arises from the mean field approximation used in the HF-method [52].

2.6 The Electron Density

In previous sections, we observed the challenges involved in solving the Schrödinger equation for larger structures. Scientists needed to come up with an approximation or model for wave function that will give logical outcome. When establishing such a model, it's worth to remember that wave function is not observable directly. Instead, we can measure is the probability that N electrons at some particular set of position $(\mathbf{r}_1, ..., \mathbf{r}_N)$. Also, we need to remember that all electrons are identical. So we can not level them as electron 1 or electron N, but we could figure out the probability of any order or set of N electrons being in the coordinates $\mathbf{r}_1$ to $\mathbf{r}_N$. Keeping this factors in mind, the electron density which is the fundamental parameter for DFT can be calculated like [56, 57]:

$$n(\mathbf{r}) = N \int d\mathbf{r}_2 ... \int \psi^*(\mathbf{r}_1, \mathbf{r}_2, ..., \mathbf{r}_N)\psi(\mathbf{r}_1, \mathbf{r}_2, ..., \mathbf{r}_N)d\mathbf{r}_N \tag{2.55}$$

The total number of electrons can be obtained by integration the electron density over the spatial variables [52]

$$N = \int n(\mathbf{r})d\mathbf{r} \tag{2.56}$$

2.7 Thomas-Fermi Model

Many people have looked into the subject of explaining the density of a assembly with multiple electrons, which led to the so-called density functional theory. The first exploration has done by Llewellyn Thomas and Enrico Fermi in 1927, which is known as Thomas-Fermi model [58]. The model helps to describe the electronic structure of many election system. It was made in a semi-classical way soon after the Schrödinger equation was made. It's a semi-classical approach since it borrows some ideas from quantum mechanics. But the rest of the ideas don't use quantum physics. Instead, they can be operated with regular function. Unlike the wave function based approach, this formulation was completely based on electronic density and is seen as a precursor to the modern DFT. The total energy of a system, within the Thomas-Fermi model, is given as a functional of density like $E_{TF}[n(\mathbf{r})]$. The Thomas-Fermi energy functional composed of three terms, is expressed as follow:

$$E_{TF} = X \int n(\mathbf{r})^{\frac{5}{3}} d\mathbf{r} + \int n(\mathbf{r})V_{ext}(\mathbf{r})d\mathbf{r} + \frac{1}{2}\int\int \frac{n(\mathbf{r})n(\mathbf{r})}{|\mathbf{r} - \mathbf{r}'|}d\mathbf{r}d\mathbf{r}' \tag{2.57}$$

The initial phase is the electronic kinetic energy of a system of electrons in a uniform electron gas that do not interact with each other. We can obtain this by integrating the kinetic energy density of a homogeneous electron gas to $t_0[n(\mathbf{r})]$ as:

$$T_{TF} = \int t_0[n(\mathbf{r})]d\mathbf{r} \tag{2.58}$$

$t_0[n(\mathbf{r})]$ is obtained by summing all the free-electron energy states $\varepsilon = \frac{P^2}{2M}$ up to the

Fermi wave vector $P_F = [3\pi^2 n(\mathbf{r})]^{\frac{1}{3}}$ given by:

$$t_0[n(\mathbf{r})] = \frac{2}{2\pi^2}\int_0^N \frac{P^2}{2M} N_P dP \tag{2.59}$$

The term N_P leads to the density of allowed states in reciprocal space given by $\frac{4\pi P^2 V^2}{h^3}$. This gives us the result for X as:

$$X = \frac{3}{10}(3\pi^2)^{\frac{2}{3}} \tag{2.60}$$

The second term represents the classical electrostatic energy of attraction between nuclei and electron. Here $V_{ext}(\mathbf{r})$ is the classic coulomb potential arising from the nuclei, given by the following expression:

$$V_{ext}(\mathbf{r}) = -\sum_{i=1}^{N} \frac{Z_i}{|\mathbf{r} - \mathbf{R}_i|} \tag{2.61}$$

And finally the third term in the energy functional represent the electron-electron interaction of the system. It is approximated by the classical coulomb repulsion between electrons. This is also known as Hartree energy. To obtain the ground state density of a system, the Thomas-Fermi equation must be minimized subjected to the constraint that the number of electron is conserved. This type of constraint minimization problem can be solved by using Lagrange multiplayer. Say, the minimization of a functional $A[X]$, subjected to the constraint $B[X]$, leads to the stationary condition:

$$\delta(A[X] - \alpha B[X]) = 0 \tag{2.62}$$

Here is a constant which is known as Lagrange multiplayer. This minimization leads to the solution of corresponding Euler equation:

$$\frac{\delta A[X]}{\delta X} - \alpha \frac{\delta B[X]}{\delta X} \tag{2.63}$$

Applying this above formula to the Thomas-Fermi model, it will give us the station-

ary condition:

$$\delta[E_{TF}[n(\mathbf{r})] - \alpha(\int n(\mathbf{r})d\mathbf{r}) - N)] = 0 \tag{2.64}$$

This yields the so-called Thomas-Fermi equation as:

$$\frac{5}{3}Xn(\mathbf{r})^{\frac{2}{3}} + V_{ext}(\mathbf{r}) + \int \frac{n(\mathbf{r}^{'})}{|\mathbf{r} - \mathbf{r}^{'}|}d\mathbf{r}^{'} \tag{2.65}$$

This above equation can be solved using iterative methods to obtain the ground state density. Thomas-Fermi model differs from other models because it is simple, easy to understand, and works for large of temperatures as well as pressures. With this model, we can use density to figure out the estimated term for kinetic energy. In orbital-free DFT, this formula for kinetic energy within Thomas-Fermi theory is also used as a part of better density approximations for kinetic energy. Though Thomas-Fermi theory contains all the necessary ingredients which paved the way to modern DFT, it has many shortcoming as well. And those shortcomings are:

• It tell how atoms will stick together. So, this idea be made up of molecules and solids.
• The estimation of kinetic energy is done in a rudimentary manner. Kinetic energy accounts for a substantial portion of the overall energy. So even small mistakes can add up to big problems.
• Oversimplified descriptions of how electrons interact with each other, which don't take into account many quantum effects.
• The correlation effect is neglected completely.

2.8 The Hohenberg-Kohn (HK) Theorems

When the Thomas-Fermi approach was first conceptualized, it was thought that the energy could be declared solely by means of its electronic density. It took more than three decades to offer a convincing argument for the validity of this idea, despite the fact that it seemed reasonable at the time. In 1964, Hohenberg and Kohn introduced theorems that established a strong logical basis for the preceding concepts, which they also proved. The idea of DFT is built upon two essential theorems provided by

Walter Kohn and Pierre Hohenberg. This theorems are known as Hohenberg-Kohn theorems [52, 59]. The theorems with their validity are given below:

2.8.1 The HK Theorem I

The Hohenberg-Kohn first theorem is:

The ground state of energy E_0 from Schrödinger equation in a presence of external potential $V(\mathbf{r})$ is a unique functional of electron density $n_0(\mathbf{r})$.

According to the first theorem, the ground-state density and the external potential correspond one to one. Since the external potential is fixed, the Hamiltonian hence the wave function Ψ is fixed by $n_0(\mathbf{r})$. The evidence in support of this theorem is straightforward. Consider the ground states of two N-electron systems that are characterised by two external potentials $V_{ext}(\mathbf{r})$ and $V_{ext}^{'}(\mathbf{r})$. These potentials differ from each other by more than just an additive constant. The corresponding Hamiltonians $\hat{H}$ and $\hat{H}'$, which have the same ground state density $n(\mathbf{r})$ but would have different ground state wave functions, Ψ and $\Psi^{'}$, with $\hat{H}\Psi = E_0\Psi$ and $\hat{H}'\Psi^{'} = E_0^{'}\Psi^{'}$. Since $\Psi^{'}$ is not the ground state of $\hat{H}$, it follows that

$$\begin{aligned} E_0 &< \langle\Psi'|\hat{H}|\Psi'\rangle \\ &< \langle\Psi'|\hat{H}'|\Psi'\rangle + \langle\Psi'|\hat{H} - \hat{H}'|\Psi'\rangle \\ &< E_0' + \int n_0(\mathbf{r})[V_{ext}(\mathbf{r}) - V_{ext}'(\mathbf{r})]d\mathbf{r} \end{aligned} \tag{2.66}$$

Similarly,

$$\begin{aligned} E_0' &< \langle\Psi|\hat{H}|\Psi\rangle \\ &< \langle\Psi|\hat{H}|\Psi\rangle + \langle\Psi|\hat{H}' - \hat{H}|\Psi\rangle \\ &< E_0 + \int n_0(\mathbf{r})[V_{ext}'(\mathbf{r}) - V_{ext}(\mathbf{r})]d\mathbf{r}. \end{aligned} \tag{2.67}$$

Adding equation (2.66) and equation (2.67)) lead to the contradiction

$$E_0 + E_0' < E_0 + E_0' \tag{2.68}$$

Hence, no two different external potential $V_{ext}(\mathbf{r})$ can give rise to the same ground

state density $n_0(\mathbf{r})$ which determines the external potential $V_{ext}(\mathbf{r})$, except for a constant. That is to say, there is a one to one mapping between the ground state density $n_0(\mathbf{r})$ and the external potential $V_{ext}(\mathbf{r})$, although the exact formula is unknown.

2.8.2 The HK Theorem II

The second Hohenberg-Kohn theorem is:

There exists a universal functional $F[n(\mathbf{r})]$ of the density independent of the external potential $V_{ext}(\mathbf{r})$, that the minimum value of energy functional $E[n(\mathbf{r})] \equiv \int n(\mathbf{r})V_{ext}n(\mathbf{r})d\mathbf{r} + F[n(\mathbf{r})]$ is the exact ground state energy of the systen and the exact ground state density $n_0(\mathbf{r})$ minimizes this functional. Thus the exact ground state energy and density are fully determined by the functional $E[n(\mathbf{r})]$ [60].

The universal functional $F[n(\mathbf{r})]$ can be written as

$$F[n(\mathbf{r})] \equiv T[n(\mathbf{r})] + E_{int}[n(\mathbf{r})] \tag{2.69}$$

where $T[n(\mathbf{r})]$ is the kinetic energy and $E_{int}[n(\mathbf{r})]$ is the interaction energy of the particles. According to variational principle [61], for any wavefunction Ψ', the energy functional $E[\Psi']$:

$$E[\Psi'] \equiv \langle \Psi' | \hat{T} + \hat{V}_{int} + \hat{V}_{ext} | \Psi' \rangle \tag{2.70}$$

has its global minimum value only when Ψ' is the ground state wavefunction Ψ_0 with the constraint that the total number of the particle is conserved. According to HK theorem I, Ψ' must correspond to a ground state with particle density $n'(\mathbf{r})$ and external potential $V'_{ext}(\mathbf{r})$, then $E[\Psi']$ is a functional of $n'(\mathbf{r})$. According to

variational principle:

$$\begin{aligned} E[\Psi'] &\equiv \langle \Psi' | \hat{T} + \hat{V}_{int} + \hat{V}_{ext} | \Psi' \rangle \\ &= E[n'(\mathbf{r})] \\ &= \int n'(\mathbf{r}) V'_{ext}(\mathbf{r}) d\mathbf{r} + F[n'(\mathbf{r})] \\ &> E[\Psi_0] \\ &= \int n_0(\mathbf{r}) V_{ext}(\mathbf{r}) d\mathbf{r} + F[n_0(\mathbf{r})] \\ &= E[n_0(\mathbf{r})] \end{aligned} \tag{2.71}$$

Thus the energy functional $E[\Psi'] \equiv \int n(\mathbf{r}) V_{ext}(\mathbf{r}) d\mathbf{r} + F[n(\mathbf{r})]$ evaluated for the correct ground state density $n_0(\mathbf{r})$ is indeed lower than the value of this functional for any other density $n(\mathbf{r})$. Therefore by minimizing the total energy functional of the system with respect to variations in the density $n(\mathbf{r})$, one would find the exact ground state density and energy. This functional only determines ground state properties, it doesn't provide any guidance concerning excited states.

2.8.3 Advantage and Disadvantage of HK Theorems

With the help of these theorems, it is possible to calculate all the ground and excited states of many-body wave-functions. Because $n(\mathbf{r})$ has a single effect on external potential, it also has a single effect on the ground state wave function, which could be found from computing the full Schrodinger equation for many bodies. It also implies, density of the ground particles entirely and exclusively influences all system attributes. The Hamiltonian resembles the electronic Hamilton operator described in the formula (2.22), which was the subject of Hohenberg and Kohn's initial investigation because it involved an electron gas. The advantage of Hohenberg-Kohn theorems is that it make the process of resolving the Schrödinger equation simpler by shifting the focus from finding a function of $3N$ variables (the wave function) to a function of three variables (the electron density). The Hohenberg-Kohn theorem utilizes the variational principle to establish the connections between potential and density.

Unfortunately, Hohenberg and Kohn's framework is precise, yet it is not very useful in practical calculations. Hohenberg and Kohn together could not offer any way to find the proper electronic density [62]. As there is no explicit formula linking the kinetic energy to the electronic density at this point, determining it accurately is the main challenge. The Laplacian of the one-body density matrix, which is not directly related to the density itself, must be known in order to calculate the kinetic energy term precisely. Because of this, it is challenging to calculate the kinetic energy precisely. The Hohenberg-Kohn theorems are limited in their applicability to ground-state systems exclusively. This means that it cannot be used to describe excited states or dynamics of a system. Another limitation is that the theorem assumes a non-degenerate ground state, which may not always be the case for certain systems.

2.9 Kohn-Sham (KS) Equation

Kohn and Sham proposed a method to solve the problems that arises in the Hohenberg-Kohn theorem [63] based on two approximations described as follows [64]:

1. The ground state density can be understood as the ground state of a system consisting of non-interacting particles in an auxiliary framework.

2. The Hamiltonian of the auxiliary system is formulated using the conventional kinetic energy operator, while the auxiliary potential is regarded as an effective local potential.

The Kohn-Sham theorem postulates that the electron density of the ground state in an interacting system is equivalent to the electron density of the ground-state in a non-interacting system, provided that an effective potential V_{eff} is employed. We disregard all forms of interaction between atoms, electrons, and nuclei in a system that doesn't interact. This approximation best works for densities which are smooth and vary slowly [63]. Kohn and Sham considered a many-body, multi electronic system composed of non-interacting particles. They solve the system using a modified form of Schrödinger equation for a non-interacting system that produces

the same value of ground state electron density as an interacting system. The non interacting wave function of a many body wave function is a Slater determinant of one electron wave function. One can obtain the wave function by solving this Schrödinger equation (also refers as Kohn-Sham equation):

$$\hat{H}_{KS}\psi_i = [-\frac{\hbar^2}{2m_e}\nabla^2] = \varepsilon_i\psi_i \tag{2.72}$$

Here, the term V_{eff} refers to effective potential, which compensates error due to ignoring interaction. The total energy $E(E = \sum_i \varepsilon_i)$ is divided into two parts. The known component which comes from the non-interacting part. As well as the unknown component which is also known as exchange-correlation part ($E_{xc}[n(\mathbf{r})]$). It contains all the errors that are contain in a non-interacting system as we neglect all types of interaction between particles. The kinetic energy term is divided into two parts: the kinetic energy of non-interacting particles (T_a) and the kinetic energy of interacting particles (T_b). The non-interacting part can be obtain by the equation:

$$T_a[n(\mathbf{r})] = -\frac{\hbar^2}{2m_e}\sum_i \langle\psi_i|\nabla^2_{\mathbf{r}_i}|\psi_i\rangle \tag{2.73}$$

The kinetic energy of interacting particles (T_b) can be obtained by approximation methods like LDA, GGA. Also, the effective potential can be obtained from:

$$V_{eff} = V_{ext} + V_{Hartree}[n(\mathbf{r})] + V_{xc}[n(\mathbf{r})] \tag{2.74}$$

Here, $V_{Hartree}[n(\mathbf{r})]$ is Hartree potential, which is obtained by:

$$V_{Hartree}[n(\mathbf{r})] = \frac{e^2}{4\pi\varepsilon_0}\int \frac{n(\mathbf{r}')}{|\mathbf{r} - \mathbf{r}'|}d\mathbf{r}' \tag{2.75}$$

And, the exchange-correlation potential $V_{xc}[n(\mathbf{r})]$ is defined as:

$$V_{xc}[n(\mathbf{r})] = \frac{\delta E_{xc}[n]}{\delta n} \tag{2.76}$$

From those considerations, the Hamiltonian becomes:

$$\hat{H}_{KS} = -\frac{\hbar^2}{2m_e}\sum_i \nabla^2_{\mathbf{r}_i} + V_{ext} + \frac{e^2}{4\pi\varepsilon_0}\int \frac{n(\mathbf{r}')}{|\mathbf{r}-\mathbf{r}'|}d\mathbf{r}' + \frac{\delta E_{xc}[n]}{\delta n} \tag{2.77}$$

The major distinction within the formulation and the Hartree formulation is the fact that the Kohn-Sham formulation involves exchange along with correlation in the effective potential.

2.9.1 Solving Khon-Shan Equation

In a condensed matter system the KS equation gives a way to obtain the exact density and energy of the ground state. The process starts with an initial electron density $n(\mathbf{r})$, usually a superposition of atomic electron density, then the effective KS potential V_{eff} is calculated and the KS equation is solved with single-particle eigenvalues and wave functions, a new electron density is then calculated from the wave functions. This is usually done numerically through some self consistent iter-

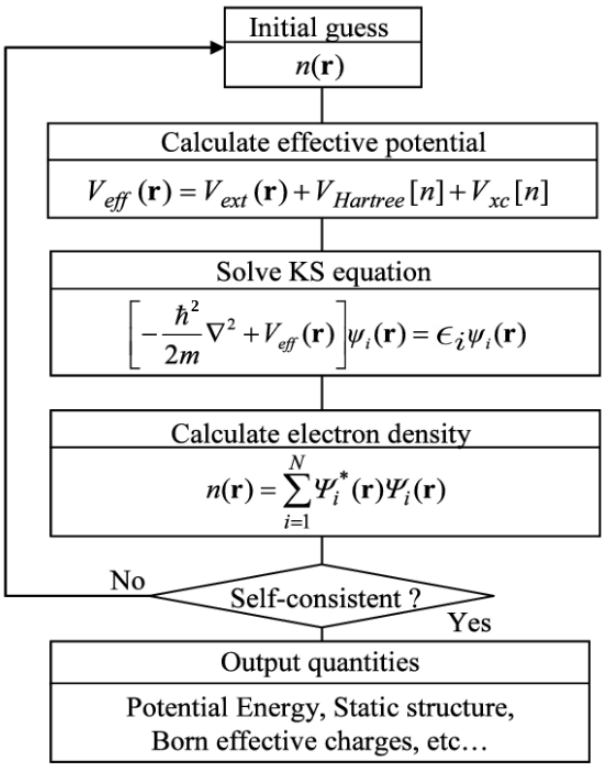

Figure 2.1: Flowchart of self-consistency loop for solving Kohn-Sham equation.

ation as shown in above flowchart. Self-consistent condition can be the change of total energy or electron density from the previous iteration or total force acting on atoms is less than some chosen small quantity, or a combination of these individual conditions. If the self-consistency is not achieved, the calculated electron density will be mixed with electron density from previous iterations to get a new electron density. A new iteration will start with the new electron density. This process continues until self-consistency is reached. After the self-consistency is reached, various quantities can be calculated including total energy, forces, stress, eigenvalues, electron density of states, band structure etc.

2.10 Exchange-Correlation (XC) Potential

In DFT, the exchange-correlation potential is a word for how the electrons in a material interact with each other. It combines the effects of exchange and correlation, which are two basic ideas in quantum physics that explain how electrons interact with each other. The exchange potential comes from the fact that electrons are identical objects and follow the Pauli exclusion principle, which says that it is impossible for two fermions that are identical to inhibit the same quantum state simultaneously. The correlation potential comes from the fact that electrons connect with each other through Coulombic forces, which depend on where and how fast they are moving. In DFT, to solve the equation (2.77), we also need an expression for the exchange-correlation potential. For the solution, different theoretical models and estimates are used to get close to the exchange-correlation potential. The accuracy of these rough estimates varies on the type of material being modeled and how it is used. In the next parts, we will talk about and analyze the local density and generalized gradient approximations, which are two of the most common ways to solve the exchange-correlation functional.

2.10.1 Local Density Approximation (LDA)

The Khon Sham equation while exactly incorporating the kinetic energy $T_a[n(\mathbf{r})]$, still leave the exchange correlational functional $E_{xc}[n(\mathbf{r})]$ unsetteled. In Khon Sham

equation let us introduce the local density approximation proposed by Khon and Sham [65]. The kinetic energy $T_a[n(\mathbf{r})]$ is regorously treated in the Kohn Sham schame, we can use the uniform electron gas formula solely for the unknown part of the rest of the energy functional. Thus we introduce the local density approximation (LDA) for exchange and correlation energy.

$$E_{xc}^{LDA}[n] = \int n(\mathbf{r})\epsilon_{xc}(n)d\mathbf{r} \tag{2.78}$$

Where, $\epsilon_{xc}[n(\mathbf{r})]$ indicates the exchange and correlation energy per particle of a uniform electron gas of density n. The corresponding exchange correlation potential then becomes,

$$V_{xc}^{LDA}(\mathbf{r}) = \frac{E_{xc}^{PBE}[n]}{\delta n(\mathbf{r})} = \epsilon_{xc}(n(\mathbf{r})) + n(\mathbf{r})\frac{E_{xc}[n]}{\delta n(\mathbf{r})} \tag{2.79}$$

and the Khon-Sham equations read,

$$[-\frac{1}{2}\nabla^2 + V(\mathbf{r}) + \int \frac{n(\mathbf{r}^{'})}{|\mathbf{r} - \mathbf{r}^{'}}d\mathbf{r}^{'} + V_{xc}^{LDA}(\mathbf{r})]\Psi = \epsilon_i\Psi_i \tag{2.80}$$

This self consistent solution defines the KS local density approximation, which is the literature is usually simply called local density approximation (LDA) method. The function $\epsilon_{xc}(n)$ can be devided into exchange and correation contributions,

$$\epsilon_{xc}(n) = \epsilon_x(n) + \epsilon_c(n) \tag{2.81}$$

The exchange part is already known given by the Dirac exchange energy functional.

$$\epsilon_x(n) = -C_x n^{\frac{1}{3}}(\mathbf{r}) \tag{2.82}$$

where,

$$C_x = \frac{3}{4}(\frac{3}{\pi})^{\frac{1}{3}} \tag{2.83}$$

2.10.2 Generalized Gradient Approximation (GGA)

The LDA neglects the inhomogeneties of the real charge density which could be very different from the homogenous electron gas (HEG). The exchange correlation (xc) energy of inhomogeneous charge density can be significantly different from the HEG result. This leads to be the development of verious generalized-gradient approximations (GGA) [66] which include density gradient corrections and higher spatial derivatives of the electron density and give better result than LDA in many cases. Three most widely used GGA's are the from proposed by Becke, Perdew et al., Burke and Enzerhof. The definition of the xc energy functional of GGA is the generalized form in the equation of LSDA to include corrections [67],

$$E_{xc}^{LSDA}[n_{\downarrow}(\mathbf{r}), n_{\uparrow}(\mathbf{r})] = \int n(\mathbf{r})\epsilon_{xc}^{home}[n_{\downarrow}(\mathbf{r}), n_{\uparrow}(\mathbf{r})]d\mathbf{r} \tag{2.84}$$

Where, xc energy density $\epsilon_{xc}^{home}[n(\mathbf{r})]$ is a function of the density alone and is composed into exchange energy density $\epsilon_{xc}^{home}[n(\mathbf{r})]$ and correlation energy density $\epsilon_{C}^{home}[n(\mathbf{r})]$. So that the xc energy functional is decomposed into exchange energy function $E_{xc}^{LDA}[n(\mathbf{r})]$ linearly. From density gradient $\nabla(\mathbf{r})$ as,

$$\begin{aligned} E_{xc}^{GGA}[n_{\downarrow}(\mathbf{r}), n_{\uparrow}(\mathbf{r})] &= \int n(\mathbf{r})\epsilon_{xc}^{home}[n_{\downarrow}(\mathbf{r}), n_{\uparrow}(\mathbf{r}), |\nabla\uparrow(\mathbf{r})|, |\nabla\downarrow(\mathbf{r})|, ...]d\mathbf{r} \\ &= \int n(\mathbf{r})\epsilon_{x}^{home}n(\mathbf{r})F_{xc}[n_{\downarrow}(\mathbf{r}), n_{\uparrow}(\mathbf{r}), |\nabla\uparrow(\mathbf{r})|, |\nabla\downarrow(\mathbf{r})|, ...]d\mathbf{r} \end{aligned} \tag{2.85}$$

Where, F_{xc} is dimensionless and $\epsilon_{xc}^{home}n(\mathbf{r})$ is the exchange energy density of the unpolarized HEG. F_{xc} can be decomposed linearly into exchange contribution F_{xc} = F_x + F_c. Generally, GGA works better than LDA, in pridicting binding energy of molecules and bond length, crystal lattice constants, especially the system where charge density varried rapidly. In case of ionic crystall, GGA overcorrects LDA results where the lattice constants of LDA fit well than GGA. But in case of transition metal oxides and rare-earth element, both LDA and GGA perform badly. This drawback leads to approximations beyond LDA and GGA.

2.10.3 Local Spin Density Approximation (LSDA)

In the majority of the exchange-correlation functionals, the homogenous electron gas is used. Particularly, in local density approximation, the density, n is considered at each point in space and the homogenous electron gas model is applied locally using the density only [68]. In the local spin density approximation (LSDA), the electron density for individual spin components, $n_\alpha(r)$ and $n_\beta(\mathbf{r})$ are used. Using the homogeneous electron gas model, the exchange energy functional is known as Dirac exchange and has a very simple mathematical form

$$E_x{}^{LSDA} = -\frac{3}{2}(\frac{3}{4\pi})^{\frac{1}{3}} \int [n_\alpha(\mathbf{r})^{\frac{4}{3}} + n_\beta(\mathbf{r})^{\frac{4}{3}}] d\mathbf{r} \tag{2.86}$$

The general form of the local spin density approximation for the correlation energy functional has the following form

$$E_c^{LSDA}[n_\alpha, n_\beta] = \int n[\mathbf{r}\varepsilon_c(n_\alpha(\mathbf{r}), n_\beta(\mathbf{r})] d\mathbf{r} \tag{2.87}$$

where, $\varepsilon_c[n_\alpha(\mathbf{r}), n_\beta(\mathbf{r})]$ is the correlation energy per electron in a homogeneous electron gas. The exact form is unknown but many approximations to $\varepsilon_c[n_\alpha(\mathbf{r}), n_\beta(\mathbf{r})]$ exist. LSDA gives fairly good results for equilibrium geometries and vibrational frequencies for covalently bonded molecules but has a tendancy to overbind atoms because the molecule is overstabilized compared to the separate atoms. Moreover, the results are bad for molecules containing hydrogen bonds and van der Waals complexes.

In LSDA, the exchange energy is typically underestimated by 10% and the correlation energy overestimated by 100%. The total energy is too high, the gap between occupied and unoccupied orbitals (or bands in solid state physic) is too low. Moreover, LSDA favor the $d^{n+1}s^1$ configuration over the $d^n s^2$ in the $3d$ transition metal atoms. Gunnarsson and Jones showed that the major source of error in LSDA comes from the exchange energy. A source of error in the calculation of the exchange energy is the self-interaction repulsion present in LSDA. This error is related to the fact that an electron sees all other electrons including itself. The presence of such an error is

easy to verify, since the exchange energy of any one-electron system should be zero. Perdew and Zunger have proposeda self-interaction corrected LSDA functional that reduced the error below 3% for the exchange energy. Improvement was also obtained in the LSDA correlation energy, in the total energy, in the orbital eigenvalues, in the long range behavior of $V_{xc}(\mathbf{r})$, in the shape of the exchange-correlation hole and consequently in the electronic density.

2.10.4 LDA+U Method

Strongly correlated system usually contain transition metal or rare-earth metal ions with partially filled d or f shells. Because of the orbital-independent potentials in LSDA and GGA, they cannot properly describe such systems. The total energy in LSDA+U method [69] is given by,

$$E_{tot}^{LDA+U}[n_\sigma(\mathbf{r}), n_\sigma] = E^{LSDA}[n_\sigma(\mathbf{r})] + E^{U}[n_\sigma] - E_{dc}[n(\mathbf{r})] \tag{2.88}$$

where, σ = spin indexes, $n(r)$ = electron density for spin-σ electrons, $n\sigma$ = density matrix of f or d electron for spin-σ electrons, $E^{LSDA}[n_\sigma(\mathbf{r})]$ = standard LSDA energy functional, and $E^{U}[n(\mathbf{r})]$ = electron-electron coulomb interaction energy. The last term is double counting term which remove the average LDA energy contribution of d or f electrons from the LDA energy

$$E_{dc}[n_(\mathbf{r})] = \frac{1}{2}UN(N-1) - \frac{1}{2}J[N_\uparrow(N_\uparrow - 1) + N_\downarrow(N_\downarrow - 1)] \tag{2.89}$$

where, $N = N_\uparrow + N_\downarrow$. U and J are coulomb and exchange parameters. If exchange and non sphericity is neglected then,

$$E_{tot}^{LDA+U} = E_{LDA} + \frac{1}{2}U\sum_{i\neq 1} n_i n_j - \frac{1}{2}UN(N-1) \tag{2.90}$$

The orbital energies ϵ_i are derivative of above equation with respect to orbital occupations n_i:

$$\epsilon_i = \frac{\partial E}{\partial n_i} = \epsilon_{LDA} + U(\frac{1}{2} - n_i) \tag{2.91}$$

For $n_i = 1$, LDA orbital energiesare shifted by $-\frac{U}{2}$ and by $\frac{U}{2}$ and by for unoccupied orbitals($n_i = 0$), resulting the upper and lower Hubbard bands, which opens a gap at the Fermi energy in transition metal oxides. In case of double counting term, it has two different treatment: around mean-field (AMF) and fully localized limit (FLL). The former is most suitable for small U system and the letter for large U system. The energies for double counting is given by,

$$E_{dc}^{AMF} = \frac{1}{2}UN^2 - \frac{U + 2lJ}{2l = 1}\frac{1}{2}\sum_{\sigma} N_{\sigma}^2 \tag{2.92}$$

and,

$$E_{dc}^{AMF} = \frac{1}{2}UN(N-1) - \frac{1}{2}J\sum_{\sigma} N_{\sigma}(N_{\sigma-1}) \tag{2.93}$$

2.10.5 Hybrid Functional

Hybrid functional approximation is a sort of computational method employed in DFT studies. It was created by A. Becke [70]. Hybrid functionals try to get around this problem by mixing parts of both the local density approximation (LDA), and the generalized gradient approximation (GGA). In this method, the first exchange-correlation energy was written in the format:

$$E_{xc}^{hyb} = \gamma E_x^{KS} + (1-\gamma)E_{xc}^{GGA} \tag{2.94}$$

Here, E_x^{KS} is the exchange energy calculated with the exact Kohn-Sham wave functions. And γ is known as fitting parameter. Currently, there are numerous popular hybrid functionals available, including B3LYP, PBE0, and HSE06. Each of these functionals has its own unique strengths and weaknesses, which depend on the specific material and property being studied. The main benefit of hybrid functionals is that they blend the best parts of both LDA and GGA functionals. LDA does a good job of describing how the density changes slowly, but it doesn't account for the exchange-correlation energy in systems where the density changes. GGA, on the other hand, gives a better picture of the exchange correlation energy, but it often overestimates or underestimates certain properties, such as band-gaps, bond

lengths, and reaction energies. Hybrid functionals get around these problems by adding a small amount of exact Hartree-Fock exchange to the normal GGA functional. This makes the predicted properties more accurate, especially for systems with big band-gaps, states that are localized, and atoms of transition metals. The result is a hybrid functional that is a mix of LDA and GGA parts. This gives a good balance between accuracy and cost of processing.

Chapter 3

Outcomes and Interpretation

Computational Details

First-principle calculations of $CaZrO_{3-x}Se_x$ ($x = 0, 1, 2, 3$) were performed using the full-potential linearized augmented plane wave (FP-LAPW) approach [71,72] as implemented in the WIEN2k code [73], which works within density functional theory (DFT) [74]. The exchange and correlation potential [75] is used within the generalized gradient approximations (GGA) scheme of Perdew-Burke-Ernzerhof (PBE) to solve Khon-Sham equation. In the full potential scheme the unit cell of the crystal is separated into two different regions: atomic spheres and interstitial site [76]. Within the atomic sphere the wave function is extended in atomic-like functions (radial part times spherical harmonics) while in the interstitial region the wave function is presented in a plane wave basis. The energy convergence function used $R_{MT}K_{max} = 8$, where, K_{max} is the size of the largest k vector in the plane wave expansion and R_{MT} is the radius of the smallest atom in the unit cell. The energy separation between core and valence states has been set to -6.0 Ry. Inside the sphere the angular momentum vector, $l_{max} = 10$, while the maximum values of the Gaussian factor, G_{max} = 16 (a.u.)$^{-1}$. The limit for energy convergence and charge convergence for the iteration process was set to 10^{-5} Ry and 10^{-3} e respectively. From the energy-volume

calculations, we found the optimal ground state parameters using the Murnaghan equation of state. The number of states that are accessible for each interval of energy per unit volume was calculated by analyzing the density of states. We have used 10×10×10 k-mesh for the Brillouin zone integration for structural and electronic properties calculations, and 20×20×20 k-mesh used for optical properties calculations. To calculate elastic constants, we used Charpin's approach as implemented in WIEN2k [77]. Finally, mechanical poperties of the $CaZrO_{3-x}Se_x$ ($x = 0, 1, 2, 3$) were calculated using second-order derivative within WIEN2k package to evaluate elastic tensor of a cubic and tetragonal phase structure. As the structure is cubic, there are only three independent constants C_{11}, C_{12}, and C_{44}. For tetragonal structure, there are six elastic constants C_{11}, C_{12}, C_{13}, C_{33}, C_{44}, and C_{66}. These independent elastic constants are used to determine the mechanical stability of $CaZrO_{3-x}Se_x$ ($x = 0, 1, 2, 3$) perovskites.

3.1 Structural Properties

$CaZrO_3$ is categorized under the spatial symmetry of the $Pm\bar{3}m$ (221) crystallographic space group and has a cubic perovskite crystal structure, as illustrated in Figure 3.1(a). The arrangement of atoms is as follows: Ca locates at the center of the unit cell at coordinates $(0, 0, 0)$, Zr occupies at the corner position $(0.5, 0.5, 0.5)$, and O resides at the center of the face $(0.5, 0.5, 0)$. We used atomic locations and the generalized gradient approximation (GGA) to achieve optimal lattice parameters and unit cell volume across all $CaZrO_{3-x}Se_x$ ($x = 0, 1, 2, 3$) crystal phases. Regarding cubic $CaZrO_3$, replacing 1 or 2 selenium atoms results in the formation of $CaZrO_2Se$ in Figure 3.1(b) and $CaZrOSe_2$ in Figure 3.1(c) respectively. Atomic locations in $CaZrO_2Se$ are as follows: Ca $(0, 0, 0)$, Zr $(0.5, 0.5, 0.5)$, O $(0.5, 0, 0.5)$ and Se $(0.5, 0.5, 0)$. For $CaZrOSe_2$, the positions of the atoms can be described as follows: Ca $(0, 0, 0)$, Zr $(0.5, 0.5, 0.5)$, O $(0.5, 0.5, 0)$ and Se $(0.5, 0, 0.5)$.

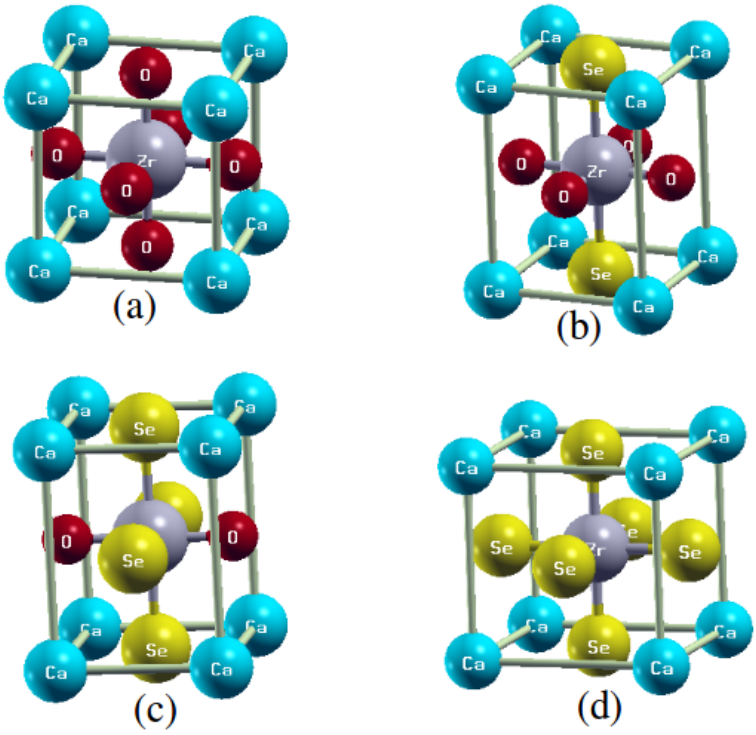

Figure 3.1: The crystal structure of compounds: a) $CaZrO_3$, b) $CaZrO_2Se$, c) $CaZrOSe_2$ and d) $CaZrSe_3$.

Importantly, this substitution instigates a change in the crystal structure from cubic to tetragonal symmetry, and the resulting phases confirm the space group $P4/mmm$ (123). Furthermore, $CaZrSe_3$ is created in the $CaZrO_3$ molecule when 3 selenide atoms are introduced as replacements shown in Figure 3.1(d). This newly formed compound has the same space group and atomic coordinates as Ca, and it still has a cubic structure similar to that. The physical characteristics and electronic band structure of the system are significantly influenced by this phase transformation. Using two cubic frameworks, $CaZrO_3$ and $CaZrSe_3$, we optimized volume and found the corresponding minimal energy volumes, which are elegantly dipicted in Figure 3.1(a), (d). The stability of these structures was evaluated, and the intricate relationship between total energy and volume was investigated, using the state equation obtained from the Birch-Murnaghan model [78]. We embarked on a two-step optimization process for the tetragonal structures, $CaZrO_2Se$ and $CaZrOSe_2$.

Table 3.1: The optimized structure information and band gap (Eg) value of $CaZrO_{3-x}Se_x$ systems.

Compounds	Space group	a (Å)	b (Å)	c (Å)	V (Å^3)	Eg (eV)
$CaZrO_3$	$Pm\bar{3}m$	4.14	4.14	4.14	252.67	3.34
$CaZrO_2Se$	$P4/mmm$	4.13	4.13	5.52	334.93	1.94
$CaZrOSe_2$	$P4/mmm$	5.35	5.35	4.01	410.38	0.71
$CaZrSe_3$	$Pm\bar{3}m$	5.23	5.23	5.23	509.18	0.23

In the initial phase, we controlled the volume while keeping the c/a ratio constant. Further refinement was achieved by maintaining the equilibrium volume while modifying the c/a ratio, an adjustment made through a parabolic fitting approach. Subsequently, employing the equation of state according to Birch-Murnaghan, we matched the resultant volume variation, elegantly displayed in Figure 3.2(b), (c). The Brich-Murnaghan's equation of state can be represented as follows:

$$E_{tot}(V) = E_0 + \frac{B_0 V}{B_0^{'}(B_0^{'}-1)}[B_0^{'}(1-\frac{V_0}{V}) + (\frac{V_0}{V})^{B_0^{'}-1}] \tag{3.1}$$

In this equation, E_0 is the energy of the ground state, B_0 is the bulk modulus and $B_0^{'}$ is its derivatives, V_0 and V are the ground state unit cell volume.

The comprehensive findings from this geometric optimization, encompassing lattice parameters and other structural intricacies for both tetragonal and cubic phases, are documented in Table 3.1. It can be seen from Table 3.1 that the lattice parameter and unit cell volume are increased when x value increasing from 0 to 3. Furthermore, the crystal formability of $CaZrO_{3-x}Se_x$ ($x = 0, 1, 2, 3$) perovskites can be evaluated by the tolerance factor (τ). The general formula of tolerance factor (τ) for cubic perovskites has been computed using the relation [31, 79]

$$\tau_{CaZrO_3} = \frac{(Ca^{2+} + O^{2-})}{\sqrt{2}(Zr^{4+} + O^{2-})} \tag{3.2}$$

and,

$$\tau_{CaZrSe_3} = \frac{(Ca^{2+} + Se^{2-})}{\sqrt{2}(Zr^{4+} + Se^{2-})} \tag{3.3}$$

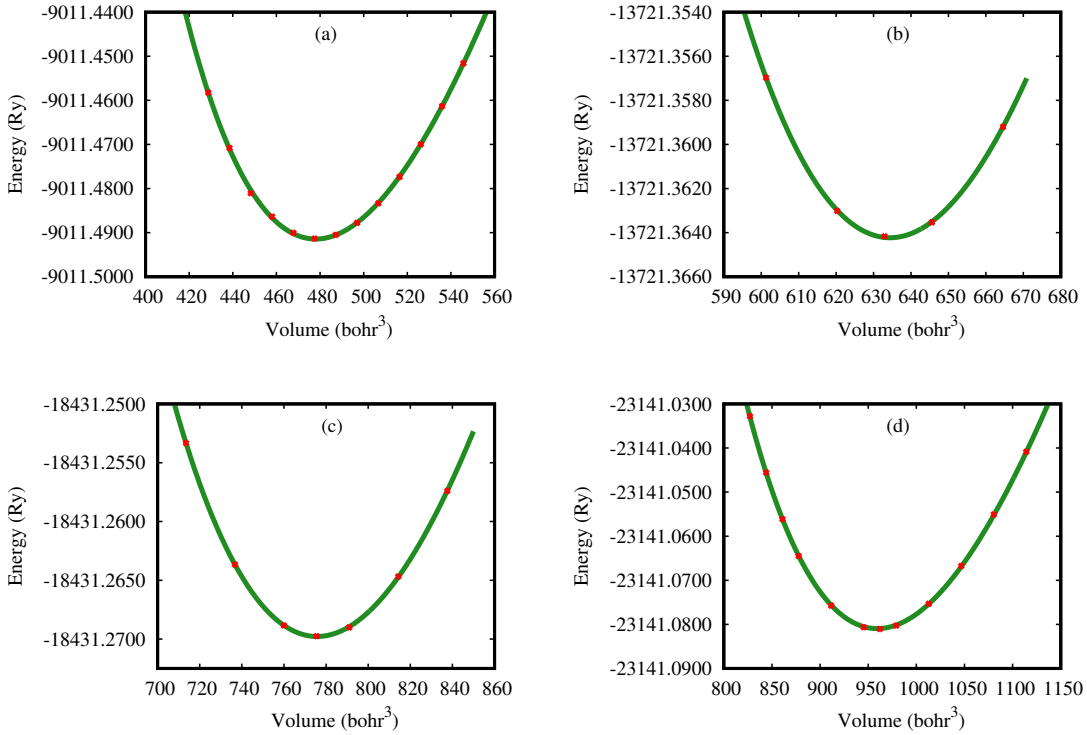

Figure 3.2: The optimization of the total energy versus unit cell volume of the studied compounds a) $CaZrO_3$, b) $CaZrO_2Se$, c) $CaZrOSe_2$ and d) $CaZrSe_3$ perovskites.

For tetragonal perovskites [80], we have used the equation

$$\tau_{CaZrO_2Se} = \frac{Ca^{2+} + \frac{2O^{2-}+Se^{2-}}{3}}{\sqrt{2}(Zr^{4+} + \frac{2O^{2-}+Se^{2-}}{3})} \tag{3.4}$$

and,

$$\tau_{CaZrOSe_2} = \frac{Ca^{2+} + \frac{O^{2-}+2Se^{2-}}{3}}{\sqrt{2}(Zr^{4+} + \frac{O^{2-}+2Se^{2-}}{3})} \tag{3.5}$$

Where, Ca^{2+}, Zr^{4+}, O^{2-}, and Se^{2-} refer to the ionic radii of Ca, Zr, O, and Se element respectively. These equations have been used to check the satbility of the studied compounds in their pure state. From Table 3.2 their tolerance factor shows that effectively such materials are found to be stable in their perovskites structure. We assessed the chemical durability of the semiconductor $CaZrO_{3-x}Se_x$ $(x = 0, 1, 2, 3)$ perovskite by determining its formation energy. The formula is given below

$$\Delta E_{form}^{CaZrO_{3-x}Se_x} = \frac{E_{total}^{CaZrO_{3-x}Se_x} - (AE_{total}^{Ca} + BE_{total}^{Zr} + CE_{total}^{Se} + DE_{total}^{O})}{A + B + C + D} \tag{3.6}$$

Table 3.2: Computed tolerance factor (τ) and formation energy (ΔE) values for each compound: $CaZrO_3$, $CaZrO_2Se$, $CaZrOSe_2$, and $CaZrSe_3$.

Compounds	Ions	Ionic radius (Å)	τ (Å)	ΔE (eV)
$CaZrO_3$	Ca^{2+}	1.14	0.82	-4.34
$CaZrO_2Se$	Zr^{4+}	0.80	0.79	-3.44
$CaZrOSe_2$	O^{2-}	1.36	0.79	-2.62
$CaZrSe_3$	Se^{2-}	1.98	0.80	-1.60

In the preceding equation, A represents the number of Ca atoms, B is the count of Zr atoms, and C and D correspond to the quantities of Se and O atoms within the unit cell respectively. $E_{total}^{CaZrO_{3-x}Se_x}$, E_{total}^{Ca}, E_{total}^{Zr}, E_{total}^{Se} and E_{total}^{O} denote the overall energies of the $CaZrO_{3-x}Se_x$ ($x = 0, 1, 2, 3$) perovskites and the stable forms of Ca, Zr, Se, and O in their solid structures, respectively. Here are the computed formation energies mentioned for the compounds: $CaZrO_3$ exhibits 4.34 eV per atom, $CaZrO_2Se$ has 3.44 eV per atom, $CaZrOSe_2$ demonstrates 2.62 eV per atom, and $CaZrSe_3$ displays 1.60 eV per atom. These values provide insight into the relative stability of these compounds, shedding light on their chemical behavior.

3.2 Electronic Properties

The electronic properties of $CaZrO_{3-x}Se_x$ ($x = 0, 1, 2, 3$) materials, such as band structure and density of states, can be elucidated by DFT computations. There are two types of electronic band gaps, direct and indirect. In direct band gap, the conduction band minima (CBM) and valence band maxima (VBM) are at same location, while in indirect band gap, CBM and VBM are at different locations. Comprehension of the electrical properties of the material requires an understanding of the band gap, which is the energy difference between conduction band and valence band. Understanding electronic band structure is also a fundamental requirement for realizing optical features. The electronic band structure via spin-polarized calculations on employing GGA method are provided in Figure 3.3. In the Brillouin zone, points of high symmetry are R(0.5, 0.5, 0.5), Γ(0, 0, 0), X(0, 0.5, 0) and M(0.5, 0.5, 0) displayed in bandstructures for $CaZrO_{3-x}Se_x$ ($x = 0, 1, 2, 3$) perovskites.

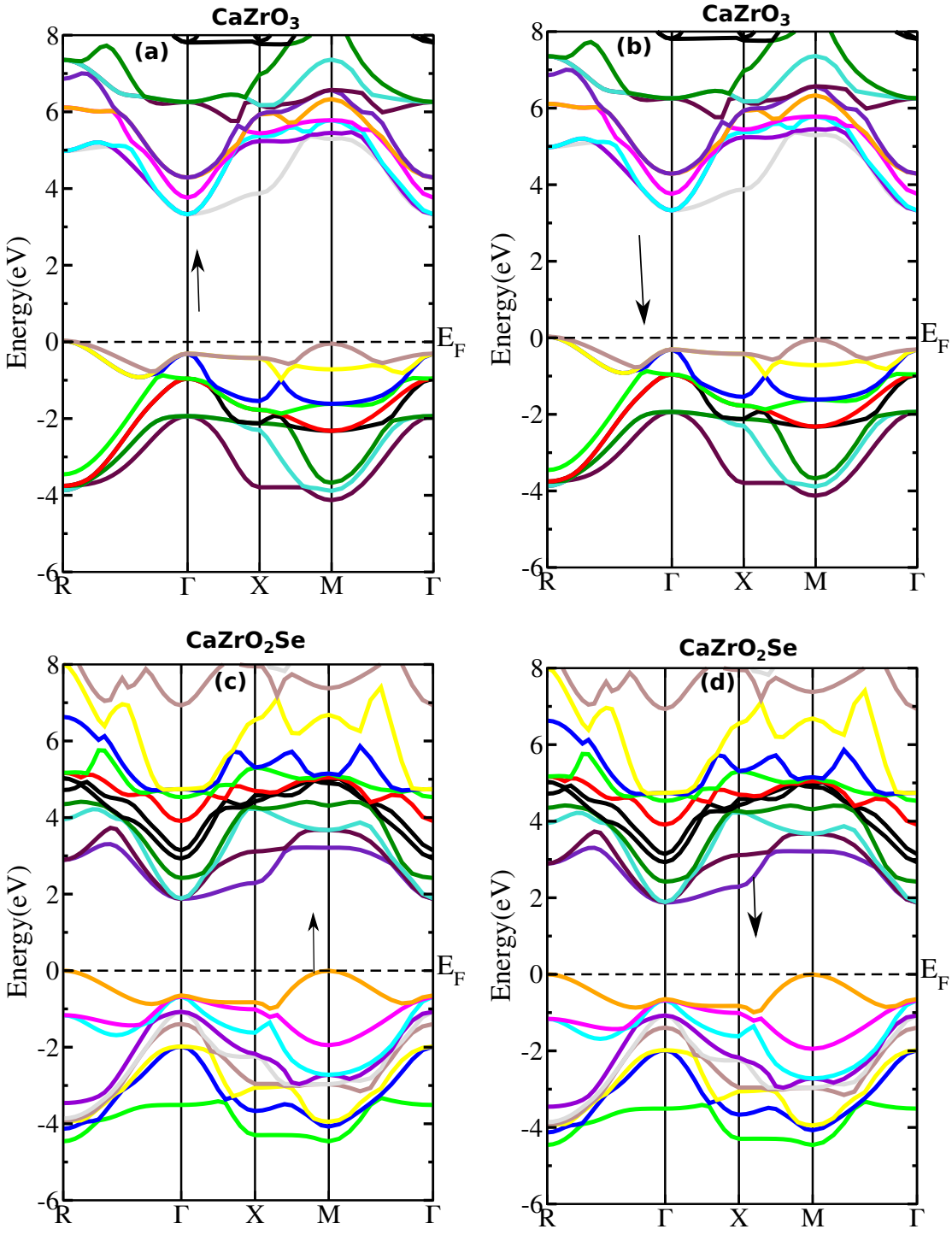
CaZrO3
(a)
(b)
CaZrO2Se
(c)
(d)
Energy(eV)
E_F
R
Γ
X
M
Γ

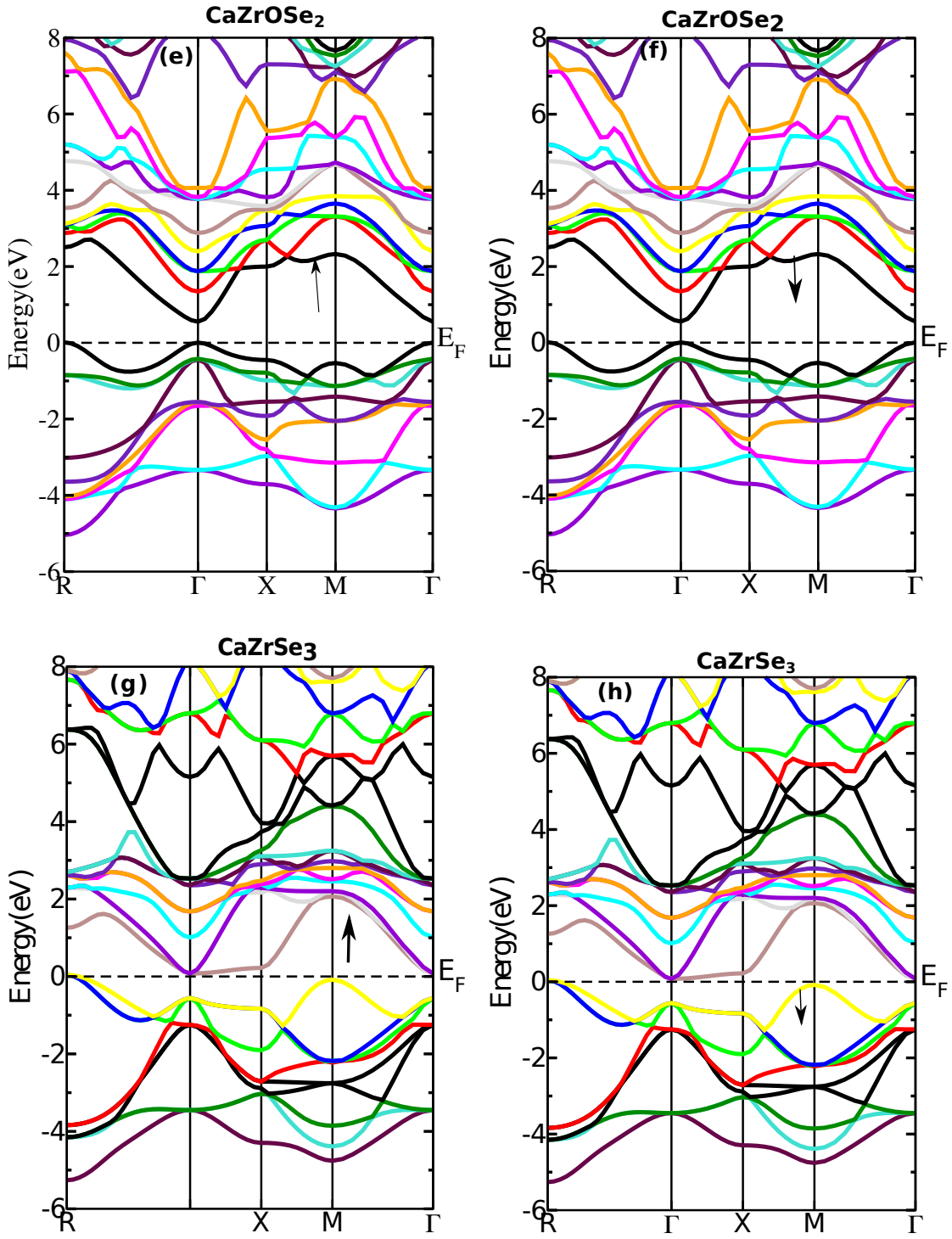

Figure 3.3: The calculated electronic band structures of $CaZrO_{3-x}Se_x$ systems a) spin-up and b) spin-down for $CaZrO_3$, c) spin-up and d) spin-down for $CaZrO_2Se$, e) spin-up and f) spin-down for $CaZrOSe_2$ and g) spin-up and h) spin-down for $CaZrSe_3$ along some high symmetry directions of brillouin zone.

It can be seen from this figure that the studied compounds are semiconductors with indirect band gap (R-Γ). It is also observed that the band gap decreases gradually from 3.44 eV to 0.23 eV, when the ratio of Se doping increases from 0 to 3 as a result of the overlapping states caused by the increasing size of chalcogens. The obtained energy band gap values are 3.44 eV, 1.94 eV, 0.71 eV and 0.23 eV for $CaZrO_3$, $CaZrO_2Se$, $CaZrOSe_2$ and $CaZrSe_3$, respectively. Again, when $x = 3$, selenium have the significant contribution comes Se-p states in the valence band regions in Figure 3.4. We assumed that selenium's influence is the main factor driving changes in the band gaps of these compounds. The calculated energy gap values are represented in Table 3.3. The suitable band gap value of 1.94 eV makes the $CaZrO_2Se$ material a potential candidate for optoelectronic application in photovoltaic. On the other-hand, the band gap energy 0.71 eV makes $CaZrOSe_2$ material a favorable candidate for photovoltaic applications. Moreover, the bandgap values of $CaZrO_3$ and $CaZrSe_3$ perovskites make them a potential candidate for other optoelectronic applications.

The investigation focused on analyzing the total and partial density of states (DOS) in order to understand more about the orbital contributions that lead to atomic bonding and the development of valence and conduction states. A strong hybridization between these orbitals is indicated by the partial density of states (PDOS) plot for $CaZrO_3$ in Figure 3.4(a), which shows that the Ca-*d*, Zr-*d*, and O-*p* states are important in creating the valence band in the deeper region. There is a noticeable

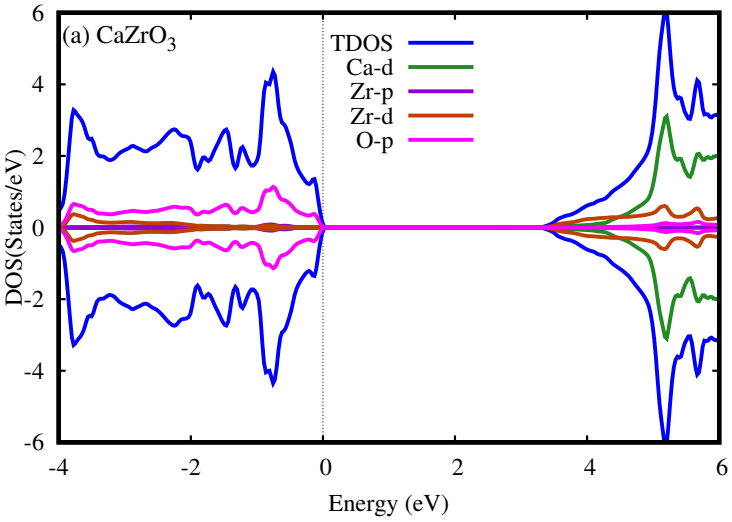

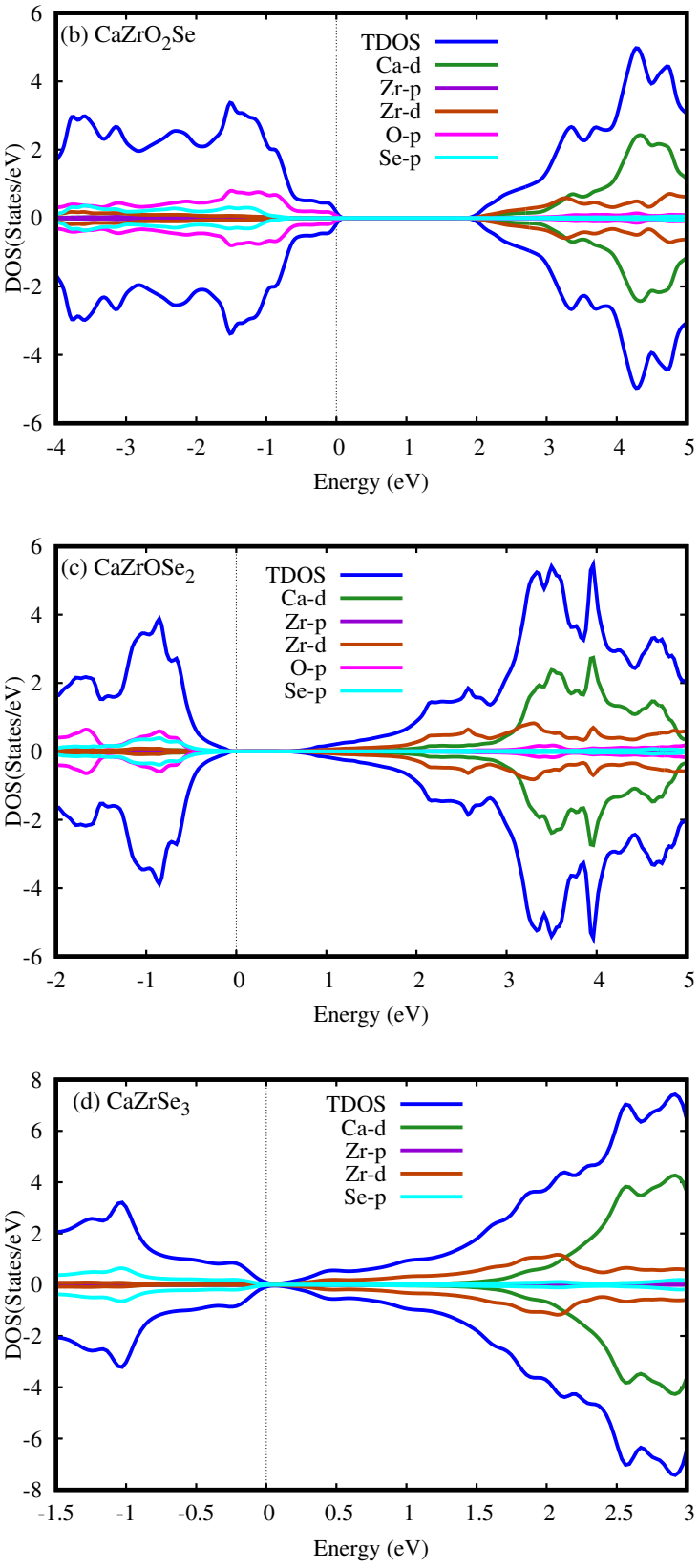

Figure 3.4: Representation of total and partial density of states (DOS) of (a) $CaZrO_3$, (b) $CaZrO_2Se$, (c) $CaZrOSe_2$, and (d) $CaZrSe_3$ systems using the GGA-PBE method.

decrease in the involvement of Ca-d states close to the Fermi level in the valence band when ($x = 1, 2, 3$) selenium atoms are substituted for $CaZrO_3$. However, this reduction is compensated by a rise in participation of Se-p states in the valence band. As a consequence, the substitution of Se for O in $CaZrO_3$ results in modifications to the electronic structure of the material, which in turn affects the functions of the atomic orbitals in the valence band. More precisely, the contribution of Ca-d states to the valence band diminishes as Se-p states start to make a substantial contribution. From this figure we can noted that the studied compounds are semiconductors along with there is no change between up spin and down spin that indicates perfect symmetry. A significant hybridization takes place between O-p and Zr-d states in the conduction band of $CaZrO_3$ at the Fermi level. At the Fermi level, Se-p states start to contribute actively and hybridize with Zr-d levels when oxygen is replaced with 1, 2, or 3 selenium atoms. Zirconium (Zr-d) is thought to have a key role in structuring the valence and conduction bands. This is because pseudo-states are produced. From Figure 3.3, we can note that the studied compounds are semiconductors. Also, the perfect symmetry between majority and minority spins indicate that the materials are non-magnetic.

3.3 Optical Properties

The optical characteristics of a material are greatly influenced by the behavior of electrons, particularly their rates of transition and recombination. Electronic transitions in semiconductor materials can be divided into two classes: intra-band and inter-band. For optical applications only inter-band transitions are responsible for excitations and recombinations [81, 82]. The optical nature of any material is explained by the imaginary dielectric function $\varepsilon(\omega)$ which describes the relationship between a material's response to incident photons and its energy given by Ehrenreich and Cohen's equation state as follows [83]:

$$\varepsilon(\omega) = \varepsilon_1(\omega) + i\varepsilon_2(\omega) \tag{3.7}$$

Here, ω denotes the angular frequency of electromagnetic radiation on the material, $\varepsilon_1(\omega)$ and $\varepsilon_2(\omega)$ indicate polarization and absorption respectively [83]. Dielectric function's imaginary part $\varepsilon_2(\omega)$ is given as follows:

$$\varepsilon_2(\omega) = \frac{4\pi^2 e^2}{m^2\omega^2}\Sigma_{i,j}\int_{Bz}\langle i|M|i\rangle^2 \times f(i)(1-f(i))\delta(E_{j,k}-E_{i,k}-\omega)d^3k. \tag{3.8}$$

Initial states are denoted by i and final states by j in this instance. The charge, electron mass, frequency, and crystal wave vector are denoted by the parameters e, m, ω, and k, respectively. As $E_{x,y}$ represents the free electron energy and M the momentum operator, $f(i)$ is the Fermi distribution function and the dielectric function's real part $\varepsilon_1(\omega)$ can be determined by using the Kramers-Kronig equation [84]:

$$\varepsilon_1(\omega) = 1 + \frac{2}{\pi}P\int_0^\infty \omega\varepsilon_2(\omega)\frac{d\omega}{\omega^2-\omega^2}, \tag{3.9}$$

where, P is the principal value of the integral. From $\varepsilon_1(\omega)$ and $\varepsilon_1(\omega)$, the following relationships are used to calculate all other optical parameters, such as refractive index $n(\omega)$, absorption coefficient $\alpha(\omega)$, optical conductivity $\sigma(\omega)$, reflectivity $R(\omega)$, and energy loss function $L(\omega)$ [84, 85].

$$n(\omega) = \frac{1}{\sqrt{2}}([\varepsilon_1^2(\omega)+\varepsilon_2^2(\omega)]^{\frac{1}{2}}+\varepsilon_1(\omega))^{\frac{1}{2}} \tag{3.10}$$

$$\alpha(\omega) = \frac{\sqrt{2}\omega}{C}([\varepsilon_1^2(\omega)+\varepsilon_2^2(\omega)]^{\frac{1}{2}}+\varepsilon_1(\omega))^{\frac{1}{2}} \tag{3.11}$$

$$\sigma(\omega) = \frac{\omega}{4\pi}\varepsilon_2(\omega) \tag{3.12}$$

$$R(\omega) = \frac{[n(\omega)-1]^2+k^2(\omega)}{[n(\omega)+1]^2+k^2(\omega)} \tag{3.13}$$

$$L(\omega) = \frac{\varepsilon_2(\omega)}{E_2^2(\omega)+E_1^2(\omega)} \tag{3.14}$$

3.3.1 Real and Imaginary Dielectric Function

The real dielectric function elaborates the dispersion and polarization of light on interaction with material of a slightly changing refractive index. The frequency of

light depends upon phase velocity which reacts to maximum dispersion and polarized light at plasma resonance of lattice waves. The values of real part, $\varepsilon_1(\omega)$ dielectric function have been depicted in Figure 3.5(a). The static dielectric function of $CaZrO_3$, $CaZrO_2Se$, $CaZrOSe_2$ and $CaZrSe_3$ are 4.0, 6.0, 9.5 and 14.5 respectively. The $\varepsilon_1(0)$ increases gradually with the change of anion oxygen to selenium. The static dielectric function is directly related to how easily the material's dipoles or charge distributions can be polarized in the presence of an electric field. It can be seen from Figure 3.5(a) that the four compounds reach peak values in the energy range of $1-3$ eV. When the ratio of Se doping increases from 0 to 3, the peak value of $\varepsilon_1(\omega)$ increase successively and go to lower energy region. The plot indicates an increasing trend with photon energy and reaches a maximum value of 8.5 (at 5 eV), 9.5 (at 3 .2 eV), 12 (at 2.5 eV), and 14 (at 1.0 eV) for $CaZrO_3$, $CaZrO_2Se$, $CaZrOSe_2$ and $CaZrSe_3$ respectively. From the peaks of maximum intensity, it becomes clear that the resonance frequency is fully polarized in a direction perpendicular to electric field of the incident light. Moreover, it shifts toward lower photon energy after increasing doping ratio. Furthermore, over the resonance, the peaks started droping to minimum value and after that entering the negative zone.

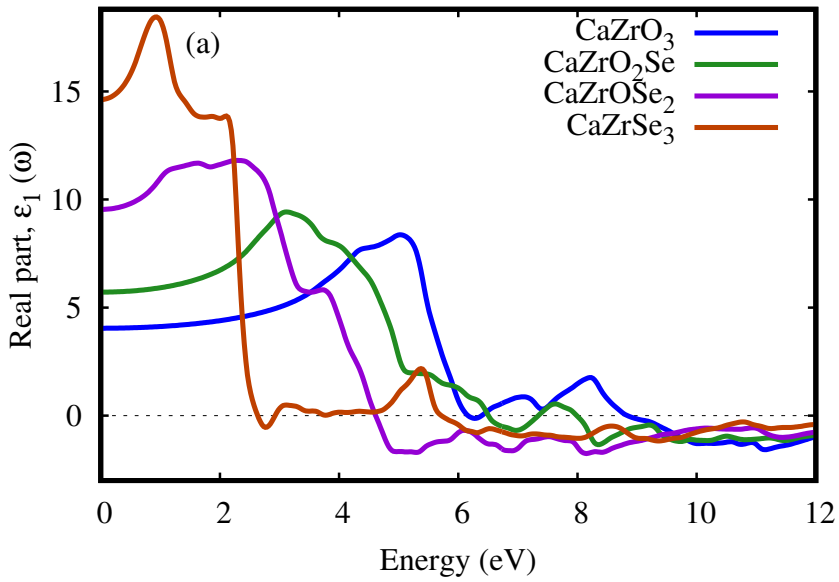

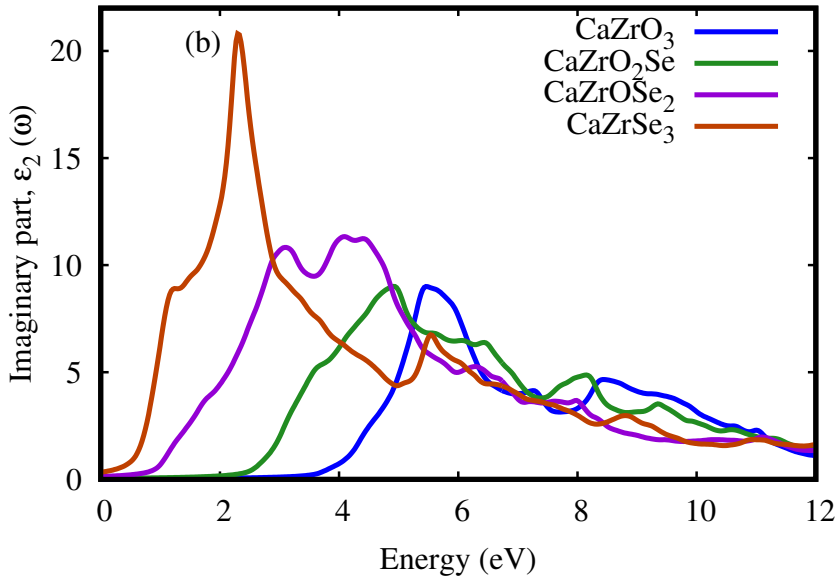

Figure 3.5: Energy versus dielectric constant of $CaZrO_{3-x}Se_x$ ($x = 0, 1, 2, 3$) perovskites.

The imaginary part of dielectric function $\varepsilon_2(\omega)$ describes the material's absorption coefficient and ability of the material to interact with electromagnetic radiation. It possesses a direct relationship with the electronic band gap. The transition of electrons between energy levels at different states leads to the formation of imaginary part of dielectric function. The imaginary part of dielectric function $\varepsilon_2(\omega)$ for $CaZrO_{3-x}Se_x$ ($x = 0, 1, 2, 3$) are plotted in Figure 3.5(b). The first peak for all compounds is caused by the transition from the valence band (primarily made up of p-orbitals) to the conduction band (made up of p and d-orbitals), when the photon's energy rises. Such transitions also related to the second peak. Imaginary part of dielectric function has large number of peak because of transition between unoccupied and occupied states of valence and conduction band as shown in Figure 3.5. From 0-3.34 eV, 0−1.94 eV, 0−0.71 eV , 0−0.23 eV no transition take place for $CaZrO_3$, $CaZrO_2Se$, $CaZrOSe_2$, and $CaZrSe_3$ respectively because incident photon has less energy than band gap between valence and conduction band. In this interval, instead of taking electron from valence band to conduction band the electron continuously radiate energy. The threshold energy for transition is around 3.34 eV, 1.94 eV, 0.71 eV and 0.23 eV. We can note that these values are closely related to the electronic band gap. We can see that there is a strong correlation between these values and the electrical band gap. Furthermore, it is evident that for $CaZrO_3$,

$CaZrO_2Se$, $CaZrOSe_2$, and $CaZrSe_3$, the $\varepsilon_2(\omega)$ reaches the greatest peaks at 5.67, 5.12, 4.10, and 2.12 eV. The values of $\varepsilon_2(\omega)$ fall negative region as energy increases due to reflection of incident light. Subsequently, the absorption start to take place and its value rises as a result of the point contributing to $\varepsilon_2(\omega)$ beginning to rise rapidly.

3.3.2 Refractive Index and Absorption Coefficient

In order to further understand the optical properties of $CaZrO_{3-x}Se_x$ $(x = 0, 1, 2, 3)$ materials, we calculated the refractive index, $n(\omega)$ of the materials from real and imaginary parts of the dielectric function. The refractive index, $n(\omega)$ is used to determine the amount of light bent or refracted as it enters into a substance. Furthermore, the phase velocity of an electromagnetic wave in a medium can be calculated by $n(\omega)$. The refractive index $n(\omega)$ reflects the dispersion of light and transparency of the materials are shown in Figure 3.6(a). According to the order in the diagram, the refractive index zero energy $n(0)$ of the $CaZrO_{3-x}Se_x$ $(x = 0, 1, 2, 3)$ compounds are 2.00, 2.40, 3.10, and 3.85 respectively. The values of static dielectric function and static refractive index are related to each other by $n^2(0) = \varepsilon_1(0)$ where, $\varepsilon(0)$ and $n(0)$ are used to find applicability to interact with light and control its propagation through the material. This is the conformation range of $n(\omega)$ from 2 to 3 is ideal for visible light solar cells. In addition to, the value of $n(0)$ has shown an increasing trend with photon energy and reaches a maximum of 3.0 at 5.4 eV for $CaZrO_3$, 3.2 at 3.4 ev for $CaZrO_2Se$, 3.56 at 2.4 eV for $CaZrOSe_2$, and 4.4 at 1.0 eV $CaZrSe_3$ respectively. After that, with further increase in photon energy, $n(0)$ declines. This implies that $CaZrO_{3-x}Se_x$ $(x = 0, 1, 2, 3)$ should be preferable for optical devices.

The optical absorption coefficient $\alpha(\omega)$ denotes the amount of energy absorbed by a substance per unit length similar to the imaginary dielectric function. This absorption behavior is influenced by various factors like the crystal's band gap and molecular structure. In particular, optical absorption happens when the frequency of incoming photons matches the atomic transition frequency within the material. Each semiconductor material has a light absorption threshold below which it

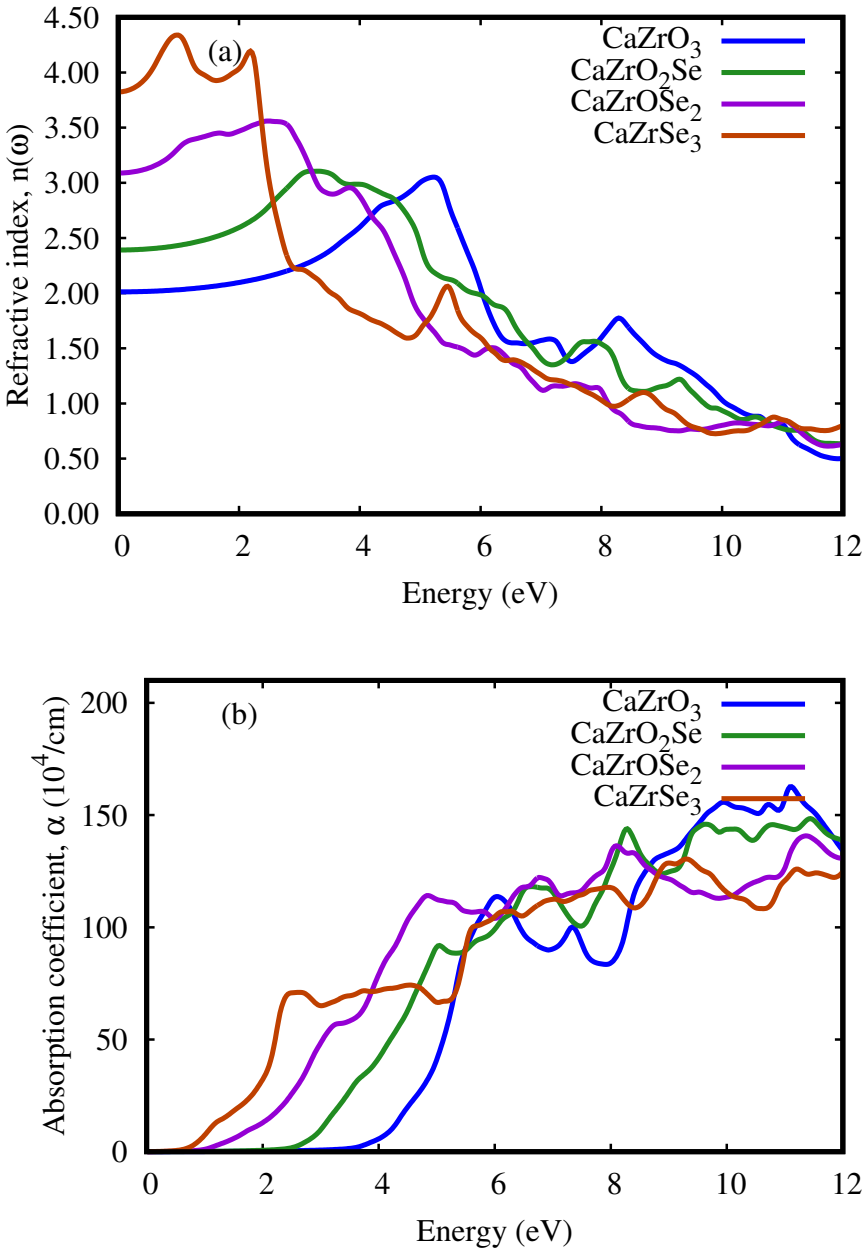

Figure 3.6: The calculated optical parameter of $CaZrO_{3-x}Se_x$ $(x = 0, 1, 2, 3)$ compounds, (a) refractive index $n(\omega)$, and (b) absorption coefficient $\alpha(\omega)$.

does not function. The interaction of photon with the valence electrons makes them capable of light absorption over this threshold limit. The relationship $\alpha = 4\pi k/\lambda$ represents the maximum rate of light degradation. Figure 3.6(b) illustrate the behavior of absorption coefficient $\alpha(\omega)$ as a function of photon energy (eV). From Figure 3.6(b) and Figure 3.5(b), both absorption coefficient and imaginary part of dielectric function are analogous to each other sinch each explains absorption of light. From the figure 3.6(b), the threshold value of $\alpha(\omega)$ appears to be 3.44 eV, 1.94 eV, 0.71 eV, and 0.23 eV for $CaZrO_3$, $CaZrO_2Se$, $CaZrOSe_2$, and $CaZrSe_3$ respectively. Below threshold energy, no absorption occurs that shows transparent energy range for the material, which correspond to the forbidden energy gaps. As the photon energy increases, the $\alpha(\omega)$ increases and reaches maximum value of 160 (at 10.8 eV), 154 (at 11.5 eV), 145 (at 11.4 eV) and 135 (at 9.0 eV) for $CaZrO_3$, $CaZrO_2Se$, $CaZrOSe_2$, and $CaZrSe_3$ respectively. This sharp increase in $\alpha(\omega)$ corresponds to limit of incident photons reaching absorption edge. The highest absorption for $CaZrO_{3-x}Se_x$ $(x = 0, 1, 2, 3)$ perovskites is observed in the ultraviolet (UV) region. Higher energy regions exhibit more variations because the electron's energy is absorbed from the incoming photons with different excitation rate. After that, when the absorption coefficient starts decreasing with further increase in photon energy (eV), revealing a semiconducting nature of computed materials.

3.3.3 Optical Conductivity and Reflectivity

The optical conductivit,y $\sigma(\omega)$ is an essential parameter that assists in identifying a material's electromagnetic response. In another explanation, the optical conductivity represents the amount of photons that travelled through the samples. When a sample is subjected to a strong electric field, it reveals the electrical conductivity, and for natural frequencies, it correlates the current density to the electric field. The optical conductivity and electrical conductivity improve with increasing photon absorption. Similar characteristics exist in optical conductivity and absorption spectra, as presented in Figure 3.7(a), owing to the escape of free carriers from the valence band to the conduction band when it absorbs energy.

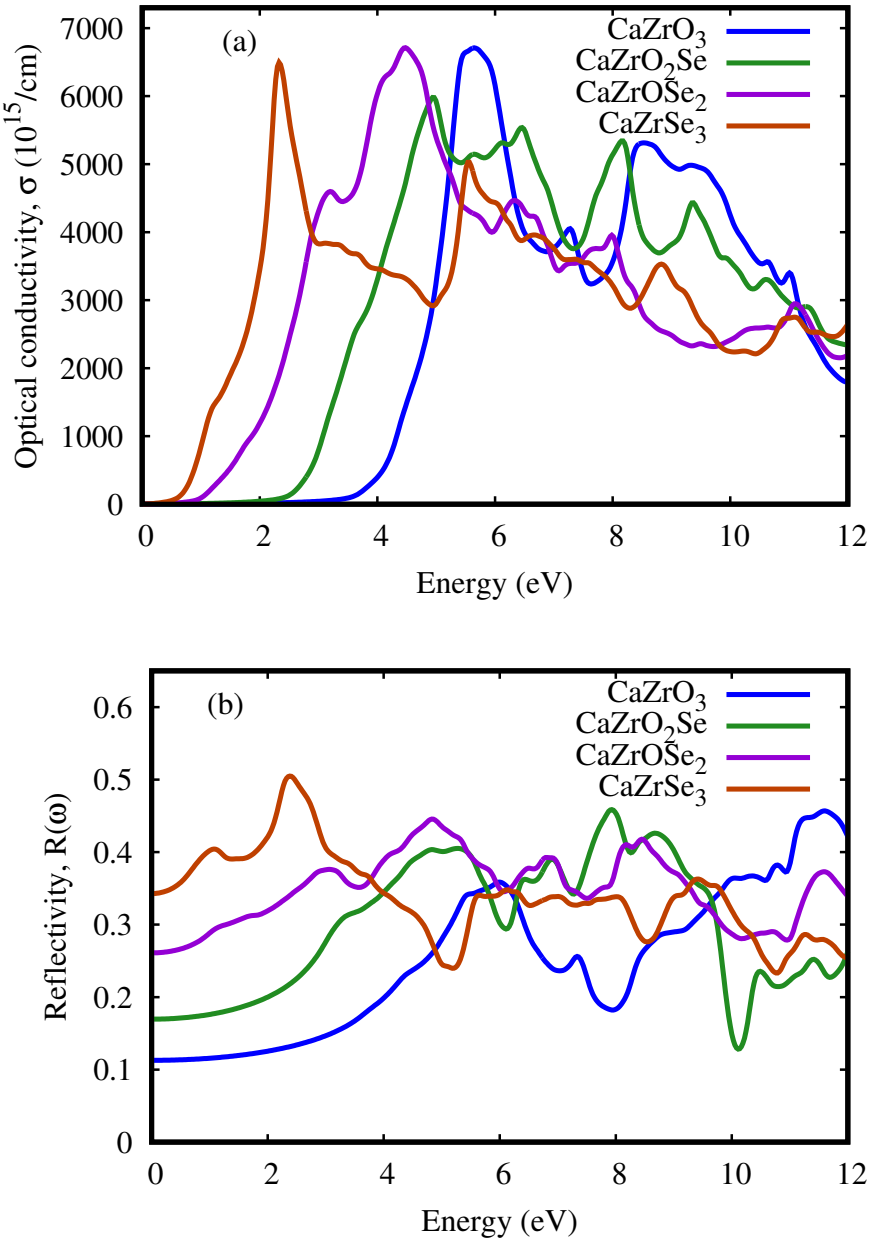

Figure 3.7: The calculated optical parameter of $CaZrO_{3-x}Se_x$ ($x = 0, 1, 2, 3$)compounds, (a) optical conductivity $\sigma(\omega)$, and (b) reflectivity $R(\omega)$.

As we can be seen in this Figure 3.7(a), the optical conductivity spectra start from 3.44, 1.94, 0.71 and 0.23 eV and reaches a maximal peak at 5.70, 4.40, 4.50, and 2.00 eV for $CaZrO_3$, $CaZrO_2Se$, $CaZrOSe_2$, and $CaZrSe_3$, respectively. Then, it decreases with certain oscillations to attain low values close to 0, which demonstrate that no electrons are found in this region. The $\sigma(\omega)$ also follow a comparable trend to that of the dielectric constants because when light of suitable frequency falls on materials surface, absorption, reflection, transmission and conduction take place simultaneously. It is also noted that the peaks of $\sigma(\omega)$ are higher for $CaZrO_2Se$ and $CaZrOSe_2$ compared to $CaZrO_3$ and $CaZrSe_3$

Reflectivity is another important optical property for the solar cell and other applications of the perovskite. The fractional amount of incident light or energy that is reflected from the surface of the surface materials can be investigated through reflectivity denoted as $R(\omega)$ as shown in Figure 3.7(b). The figure shows that under the band-gap energy, $CaZrO_{3-x}Se_x$ $(x = 0, 1, 2, 3)$ perovskites has reflectivity of the incident light. After passing through the band-gap energy, it suddenly gives a bigger pick with increasing energy and move on. In the visible region, both compounds exhibit small reflection values, which are considered to minimal influence on the efficiency of a device. However, at higher energys beyond 9 eV, the reflectivity displays larger values due to the presence of negative $\varepsilon_1(\omega)$ in that range. The low reflectivity values suggest that these materials can be effectively employed as absorbing materials in solar cells and as coating materials to minimize reflections.

3.3.4 Energy Loss Function and Extinction Coefficient

Another important factor is to measure energy loss function denoted as $L(\omega)$ which represents inter-band, intra-band, and plasmonic interactions. The energy loss function, $L(\omega)$ describes loss of energy of the first electron passing through a material. It is associated with the collective oscillation frequency of the valance electron. Moreover, the optical loss is a measure of energy loss through scattering, dispersing, and heating, as illustrated in Figure 3.8(a). In the electron energy loss function plots for $CaZrO_{3-x}Se_x$ $(x = 0, 1, 2, 3)$ compounds, the presence of peaks indicates light

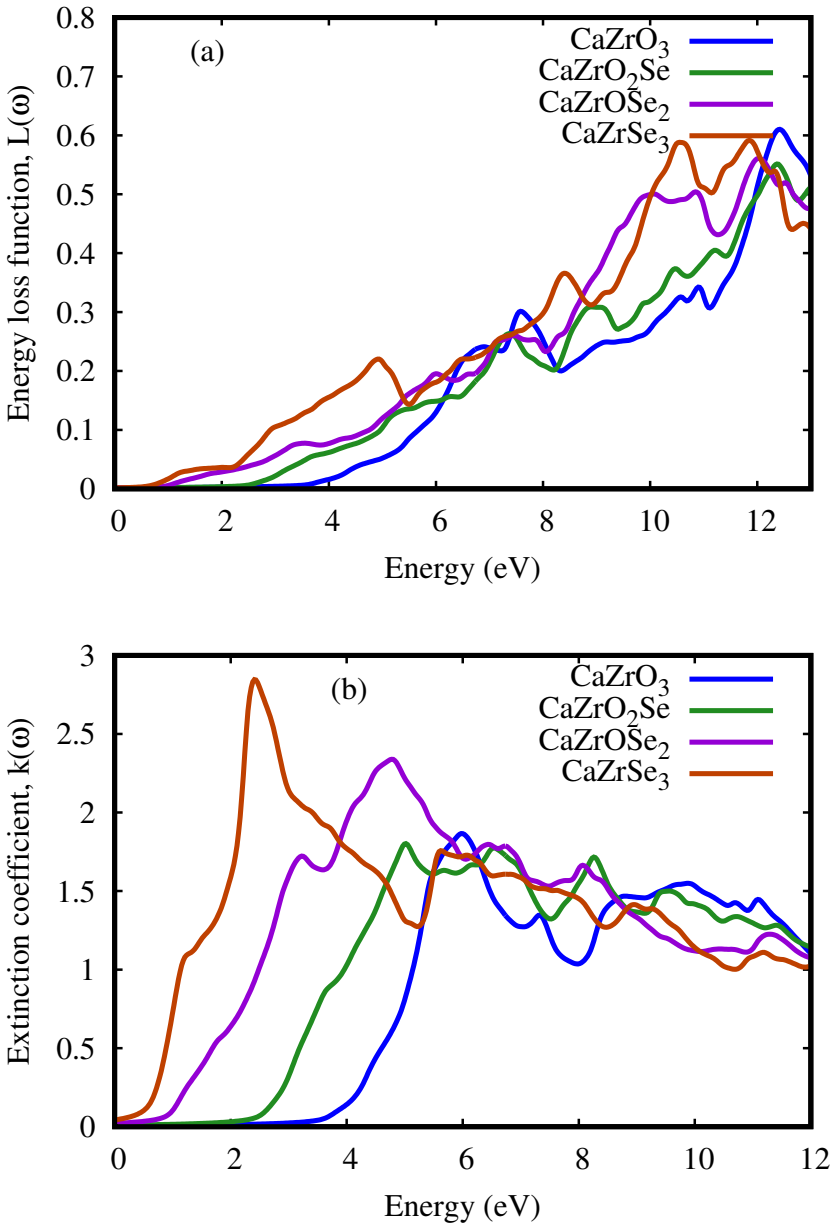

Figure 3.8: The calculated optical parameter of $CaZrO_{3-x}Se_x$ $(x = 0, 1, 2, 3)$ compounds (a) Energy loss function, $L(\omega)$ and (b) extinction coefficient, $k(\omega)$.

generated characteristic energy of excitions. Typically, this energy loss phenomenon initiates within the energy limit of approximately 0.23−3.5 eV for all studied compounds. Peaks in energy loss function, $L(\omega)$ provides an overview of plasma resonance and its corresponding frequencies, also known as plasma frequencies. Importantly, the plots show no scattering events occurs at energies lower than the materials bandgap. Interestingly, in the visible region, the value of optical loss is almost negligible (1.77−3.10 eV) as compared to in the ultraviolet region (3.10−12 eV) for $CaZrO_{3-x}Se_x$ $(x = 0, 1, 2, 3)$ perovskites respectively, confirming the studied materials suitability in visible domain of electromagnetic spectrum to realize excellent optoelectronic applications.

The extinction coefficient, $k(\omega)$ of a material provide insights into its capability to absorb incoming photons and its speed, respectively [86]. The parameter can be expressed as:

$$k(\omega) = \frac{1}{\sqrt{2}}(\sqrt{[\epsilon_1^2(\omega) + \epsilon_2^2(\omega)] - \epsilon_1(\omega)})^{\frac{1}{2}}. \tag{3.15}$$

The extinction coefficient, $k(\omega)$ shows the attenuation of light like imaginary part of dielectric function [87]. In Figure 3.8(b), the graph demonstrates the extinction coefficient, $k(\omega)$ for $CaZrO_{3-x}Se_x$. For all the compounds, $k(\omega)$ remains at 0 within the energy band gap range. As the light energy is greater than the energy band gap, the maximum values for all compounds occur between 1.5 eV and 7 eV.

3.4 Mechanical Properties

The measurement of elastic constants is essential to investigate a material's elastic properties since they define how a material response to external forces and shed light on its mechanical properties. The mechanical toughness and stability of a material are thus exposed by such constants. The Charpin approach was used to calculate elastic constants for a cubic crystal with three independent constants C_{11}, C_{12} and C_{44}, where C_{11} represents the stiffness of materials against their strains, C_{12} indicates the materials shear stress, and C_{44} signifies the resistance against shear deformation. While the tetragonal phases perovskites have more additional inde-

pendent elastic constants C_{33}, C_{66} and C_{16}. These constants can be used to relate the mechanical response to the ductility or fragility of a material when it deforms in an elastic domain. In this work, the elastic constants for $CaZrO_{3-x}Se_x$ perovskites were examined using the GGA functional. The calculated elastic constants of the studied compounds are represented in Table 3.3.

Table 3.3: Calculated elastic constant of $CaZrO_{3-x}Se_x$ ($x = 0, 1, 2, 3$) perovskites.

Parameters	$CaZrO_3$	$CaZrO_2Se$	$CaZrOSe_2$	$CaZrSe_3$
C_{11}	264.54	263.39	136.23	131.72
C_{12}	118.19	107.28	50.13	23.31
C_{13}	-	22.89	10.07	-
C_{33}	-	131.37	256.22	-
C_{44}	89.06	49.40	20.81	12.00
C_{66}	-	92.61	30.66	-

For cubic symmetry systems $CaZrO_3$ and $CaZrSe_3$, the examined elastic constants are positive which meets with the Born stability criteria [88] $C_{11} > 0$, $C_{12} > 0$, $C_{44} > 0$, $C_{11} + 2C_{12}) > 0$, $C_{11} - C_{12} > 0$, and $B > 0$ a mechanically stable state for both of the chosen materials is predicted. $C_{11} > |C_{12}|$, $2C_{13}^2 < C_{33}(C_{11} + C_{12})$, $C_{44} > 0$ and $C_{66} > 0$ are the mechanical stability condition [89] for tetragonal $CaZrO_2Se$ and $CaZrOSe_2$. The calculated elastic constant shows that the studied compounds are mechanically stable. The elastic constants were then used to calculate the elastic moduli i.e. bulk modulus (B), shear modulus (G), and Young's modulus (Y) by the Hill's formula [90], which is the average of Voight and Reuss assumptions as follow

$$B = \frac{B_V + B_R}{2}, \tag{3.16}$$

where, B_V and B_R denote the Voight and Reuss bulk moduli respectively.

The bulk modulus (B) is the measure of how resistant to compression the material is therefore the larger the bulk modulus, the better the resistant to volume deformation. The bulk modulus for cubic structure is a linear combination of C_{11} and C_{11}, so we can write [91]

$$B = \frac{C_{11} + 2C_{12}}{3}. \tag{3.17}$$

In case of tetragonal system, the bulk modulus were calculated by the following equation [92]

$$B = \frac{2(C_{11} + C_{12}) + C_{33} + 4C_{13}}{9}. \tag{3.18}$$

The bulk modulus of $CaZrO_{3-x}Se_x$ ($x = 0, 1, 2, 3$) compounds changes with the change of x value. Among the studied compounds, $CaZrO_3$ have higher B value of 166.98 GPa while $CaZrSe_3$ recorded lowest value 59.45 GPa of B.

The shear modulus (G) was estimated by Hill using Voigt's (G_V) and the Reuss's (G_R) approximations for the cubic phase structure [93]

$$G_V = \frac{1}{5}(C_{11} - C_{12}) + 3C_{44}. \tag{3.19}$$

$$G_R = \frac{5C_{44} \times (C_{11} - C_{12}}{4C_{44} + 3C_{11} - C_{12})}. \tag{3.20}$$

$$G = \frac{G_V + G_R}{2}. \tag{3.21}$$

And the following equations of shear modulus (G) for tetragonal phase structures [93] is

$$G_V = \frac{C_{11} + C_{12} + 2C_{33} - 4C_{13} + 12C_{44} + 12C_{66}}{30} \tag{3.22}$$

$$G_R = \frac{\frac{5}{2}[(C_{11} + C_{12})C_{33} - 2C_{13}^2]C_{44}C_{66}}{3BC_{44}C_{66} + [(C_{11} + C_{12})C_{33} - 2C_{13}^2](C_{44} + C_{66})} \tag{3.23}$$

$$G = \frac{G_V + G_R}{2} \tag{3.24}$$

The ability of a material to withstand transverse deformations is measured by its shear modulus, which is a function of its hardness. The high shear modulus demonstrates that the material cannot be easily changed in shape. Table 3.4 makes this

quite evident of all studied compounds, the $CaZrSe_3$ compound have the least capacity to resist shape change, with a shear modulus (G) value of 28.88 GPa. Materials with high B and G values have high melting points, which suggests that $CaZrO_3$ would have a higher melting point than $CaZrO_{3-x}Se_x$ ($x = 0, 1, 2, 3$) compounds.

The ratio of the linear stress to the strain is known as the Young's modulus (Y). Larger values of Y indicate that the material is stiffer. Young's modulus, (Y) is calculated in terms of shear (G) and bulk modulus (B) as follows [93],

$$Y = \frac{9BG}{3B + G}. \tag{3.25}$$

Table 3.4: Calculated bulk modulus B (GPa), shear modulus G (GPa), Young's modulus Y (GPa), Poission ratio ν, Cauchy pressure P_C (GPa), Pugh ratio k, anisotropy A, Kleinman parameter η, and Debye temperature θ_D (K) for $CaZrO_{3-x}Se_x$ ($x = 0, 1, 2, 3$) perovskites.

Parameters	$CaZrO_3$	$CaZrO_2Se$	$CaZrOSe_2$	$CaZrSe_3$
B	166.98	107.15	74.36	59.45
G	82.70	71.96	45.02	28.88
Y	212.95	176.38	112.37	74.57
ν	0.29	0.23	0.25	0.29
P_C	29.14	57.88	29.95	11.13
k	2.03	1.43	1.93	2.57
A	1.22	0.63	0.48	0.22
η	0.58	0.55	0.45	0.33
θ_D	607.33	494.34	342.45	253.72

Another factor is the Poisson ratio (ν) is a measure of the elastic behavior of a material under load, representing how much a material contracts in the perpendicular direction when stretched. ν gives the information about the hardness and stiffness of material. For cubic and tetragonal systems, Poisson's ratio can be drived from

the elastic moduli using the following equation [94]

$$\nu = \frac{3B - 2G}{2(3B + G)}. \tag{3.26}$$

where, B is bulk modulus and G is shear modulus. In cubic systems, the symmetry is relatively high, and the poission ratio is opten isotropic (the same in all direction). For materials with a cubic crystal structure, the typical range of Poission ratio is $0.20 \leq \nu \leq 0.30$ exhibits a mix of ionic and covalent character. The lower end of the range suggests more ionic character, while the higher end may indicate some covalent character [95]. Tetragonal systems are less symmetric than cubic systems, and the elastic properties can vary more significantly in different directions. The Poission ratio for tetragonal structures typically falls within the range $0.25 \leq \nu \leq 0.35$ [95]. In this range the presence of covalent bonding is typically stronger due to the distortion in the structure, resulting in slightly higher Poission ratios compared to cubic perovskites. The lower end of this range indicates increased anisotropy and potentially more brittle behavior. The calculated values of ν are 0.29, 0.23, 0.25 and 0.29 for $CaZrO_3$, $CaZrO_2Se$, $CaZrOSe_2$, and $CaZrSe_3$ respectively. Therefore, all the studied compounds possess ionic bonding while $CaZrO_2Se$ is covalently bonded compounds.

Cauchy pressure (P_C) is a concept derived from the stress-strain relationship in materials. It's useful in understanding the ductility or brittleness of materials based on their elastic constants. It is calculated as the difference between the elastic constants C_{12} and C_{44} for both cubic and tetragonal phase systems [80]:

$$P_C = C_{12} - C_{44} \tag{3.27}$$

The Cauchy pressure helps in predicting the mechanical behavior of materials. Its positive value indicates ductile behavior, while negative values signifies the brittle nature of the materials. Pugh ratio (k) also describes the ductile and brittleness behavior of the material based on its elastic properties [96]. It is defined as the ratio

of the bulk modulus (B) to the shear modulus (G):

$$k = \frac{B}{G} \tag{3.28}$$

For a materials, high Pugh ratio ($k > 1.75$) suggests ductile behavior, while a low ratio ($k < 1.75$) indicates brittle behavior [96]. Whether elastic anisotropy factor, (A) is a very significant parameter in engineering and the manufacturing area. Anisotropic factor measures the degree of anisotropy in a crystal's elastic properties. It is derived from the elastic constants of the material and help to describe the variation of elastic response in different crystallographic directions. The material is isotropic or anisotropic is determined by the expected value of anisotropy factor, (A). When $A > 1$, that indicates greater anisotropy, with a stiffer response in some crystallographic directions. $A < 1$ also implies anisotropy, but with a different directional dependence of elastic stiffness and $A = 1$ represents a perfectly isotropic elastic material. Both cubic and tetragonal system's anisotropy factor (A) can be calculated by the following formula [97, 98]

$$A = \frac{2C_{44}}{C_{11} - C_{12}} \tag{3.29}$$

where, C_{11}, C_{12}, and C_{44} are the elastic constants of cubic and tetragonal systems. Both of these oxide perovskites are anisotropic based on the values calculated for them, which are 1.22 for $CaZrO_3$, 0.63 for $CaZrO_2Se$, 0.48 for $CaZrOSe_2$ and 0.22 for $CaZrSe_3$. It helps to determine the microcracks within the material.

Furthermore, we have also computed the Kleinman parameter (η), which describes the relative positions of the cation and anion sub-lattices under volume-conserving strain distortions for which positions are not fixed by symmetry using the following relation for cubic and tetragonal system [98]

$$\eta = \frac{C_{44} - C_{12}}{C_{44} + C_{12}}. \tag{3.30}$$

where, C_{44} is the shear modulus and C_{12} is the elastic modulus relating to longitudinal strain. It is known that a low value of η implies that there is a large resistance

against bond bending or bond-angle distortion and vice versa. The Kleinman parameter for cubic perovskites generally ranges from -0.2 to 0.5 [99], indicating a tendency toward isotropy and for tetragonal perovskites the ranges from -0.3 to 0.5 [100], reflecting their anisotropic nature. The computed values of η are tabulated in Table 3.4.

Debye temperature (θ_D) is a characteristic temperature that provides insights into the vibrational properties of solid, including its heat capacity and thermal conductivity. It is related to the elastic constants and density of the material and can be calculated using the material's sound velocity. Debye temperature (θ_D) of the compound can be understood by utilizing the Anderson model based on elastic constants. The cubic and tetragonal perovskites having general equation for the Debye temperature (θ_D) is [101]

$$\theta_D = \frac{h}{K_B}[\frac{3n}{4\pi V}]^{\frac{1}{3}}\nu_m. \tag{3.31}$$

Here, h represents Planck's constant, V denotes the volume per atom, K_B implies Boltzmann's constant, n is the number of atoms per formula unit and ν_m is the average sound velocity in the material. The average sound velocity (ν_m) is related to the transverse (ν_t) and longitudinal (ν_l) sound velocities that can be expressed as [101]

$$\nu_m = [\frac{1}{3}(\frac{2}{\nu_t^3} + \frac{1}{\nu_l^3}]^{-\frac{1}{3}} \tag{3.32}$$

To calculate the transverse (ν_t) and longitudinal (ν_l) sound velocities, we use the following relations based on the elastic constants and density (ρ) which are determined using the bulk (B) and shear (G) modulus through Navier's equation [101]

$$\nu_t = [\frac{G}{\rho}]^{\frac{1}{2}}, \tag{3.33}$$

and

$$\nu_l = [\frac{3B + 4G}{3\rho}]^{\frac{1}{2}}. \tag{3.34}$$

For cubic perovskites, the elastic moduli C_{11}, C_{12}, and C_{44} and density can be used to estimate the Debye temperature. The Debye temperature for cubic perovskites generally falls within the range of 300 K to 800 K [102], depending on the specific ma-

terial's elastic properties. For tetragonal perovskites, the anisotropy of the crystall leads to more variation in sound velocities. Tetragonal systems exhibit differences between their elastic constant along different crystallographic axes, which affects ν_t and ν_l, and hence the Debye temperature. The Debye temperature for tetragonal perovskites is often slightly lower than that of cubic perovskites and typically falls in the range of 200 K to 600 K [103]. The computed Debye temperature, acoustic velocity of the $CaZrO_{3-x}Se_x$ ($x = 0, 1, 2, 3$) compounds, are presented in Table 3.4. Our findings suggest that substituting Se results in a decrease in the Debye temperature. Typically, harder solids exhibit higher θ_D, and a low value of θ_D indicates low lattice thermal conductivity and low minimum thermal conductivity [104]. $CaZrO_3$ has the highest values θ_D, while $CaZrSe_3$ has the lowest. The sequence of θ_D values is as follows: $CaZrO_3 > CaZrO_2Se > CaZrOSe_2 > CaZrSe_3$. The average speed of sound in these compounds also reflects this pattern.

Furthermore, the melting temperatures (T_M) in the cubic and tetragonal phases can be determined using the following equations,

$$T_M = [533 + (5.91)C_{11}], \tag{3.35}$$

and

$$T_M = 3C_{11} + 1.5C_{33} + 354, \tag{3.36}$$

for cubic and tetragonal system, respectively. Here, C_{11} and C_{33} represent the elastic constants [105–107]. When we compare these calculated T_M values, we observe that $CaZrO_3$ has a higher melting temperature than $CaZrO_2Se$, $CaZrOSe_2$ and $CaZrSe_3$ compounds. This suggests that $CaZrO_3$ is better suited for high-temperature applications. This observation aligns with the behavior of Young's modulus, as T_M and Young's modulus exhibit a strong correlation. We computed the melting temperatures of these compounds as follows: $CaZrO_3$ (2121.71 K), $CaZrO_2Se$ (2114.90 K), $CaZrOSe_2$ (1520.92 K), and $CaZrSe_3$ (1334.00 K).

Chapter 4

Conclusions

We have investigated the structural, mechanical, electronic, and optical properties of $CaZrO_{3-x}Se_x$ $(x = 0, 1, 2, 3)$ perovskite semiconducting materials using generalized gradient approximation. Selenium substitution for oxygen resulted in a remarkable structural transformation, shifting from cubic to tetragonal phases in $CaZrO_2Se$ and $CaZrOSe_2$, subsequently returning to a cubic phase in $CaZrSe_3$. The stability of these phases were confirmed by tolerance factor and negative formation energy. The semiconducting nature of the electronic density of states and band structure studies have been emphasized by the noticeable band gap between the valence and conduction bands around the Fermi level. Indirect band gap value of 3.44 eV, 1.9 eV, 0.71 eV and 0.23 eV have been observed in $CaZrO_{3-x}Se_x$ $(x = 0, 1, 2, 3)$ compounds, that are drastically reduced by Se substitution at the O sites. The optical properties demonstrated significant absorption coefficients in the order of 10^4 cm^{-1}, indicating strong light-absorbing capabilities, and they aligned closely with the band structure analysis. These materials were well suited for optoelectronic devices due to their absorption in the visible and ultraviolet region with extremely low optical loss. Further indication of their potential came from their minimal reflection and the refractive index of the studied compounds shows the optimal range of polarization and transparency for photovoltaic applications like solar cells.

Conclusions

Mainly, $CaZrO_2Se$ and $CaZrOSe_2$ emerged as promising candidates for solar cell technology, with expected light absorption in the near-infrared range to ultraviolet. The Debye temperature and melting temperature were both significantly reduced by the Se substitution in terms of elastic properties. According to an assessment of the compound's mechanical properties confirmed that $CaZrO_3$, $CaZrOSe_2$, and $CaZrSe_3$ exhibit ductile characteristics, while $CaZrO_2Se$ displays brittle behavior.

List of Abbreviations

AMF	:	Around Mean-Field
BO	:	Born-Oppenheimer
BZ	:	Brillouin Zone
CB	:	Conduction Band
CBM	:	Conduction Band Minima
DFT	:	Density Functional Theory
DOS	:	Density of States
FLL	:	Fully Localized Limit
FP-LAPW	:	Full-Potential Linearized Augmented Plane Wave
GGA	:	Generalized Gradient Approximation
HEG	:	Homogenous Electron Gas
HF	:	Hartree Fock
HK	:	Hohenberg-Kohn
KS	:	Kohn-Sham
LDA	:	Local Density Approximation
LSDA	:	Local Spin Density Approximation
PBE	:	Perdew-Burke Ernzerhof
PDOS	:	Partial Density of States
RHF	:	Restricted Hartree Fock
ROHF	:	Restricted Open-Shell Hartree Fock

SOC	:	Spin Orbit Coupling
UV	:	Ultraviolet
VB	:	Valence Band
VBM	:	Valence Band Maxima
XC	:	Exchange Correlation

Bibliography

[1] Shakeel Ahmad Khandy and Dinesh C Gupta. Investigation of structural, magneto-electronic, and thermoelectric response of ductile $SnAlO_3$ from high-throughput DFT calculations. *International Journal of Quantum Chemistry*, 117(8):e25351, 2017.

[2] Ali M Huerta-Flores, JM Mora-Hernández, Leticia M Torres-Martínez, Edgar Moctezuma, D Sánchez-Martínez, María E Zarazúa-Morín, and Björn Wickman. Extended visible light harvesting and boosted charge carrier dynamics in heterostructured zirconate FeS_2 photocatalysts for efficient solar water splitting. *Journal of Materials Science: Materials in Electronics*, 29:18957–18970, 2018.

[3] Xia Li and Jinling Zang. Hydrothermal synthesis and characterization of lanthanum-doped $NaTaO_3$ with high photocatalytic activity. *Catalysis Communications*, 12(14):1380–1383, 2011.

[4] I Hamideddine, H Zitouni, N Tahiri, O El Bounagui, and H Ez-Zahraouy. A DFT study of the electronic structure, optical, and thermoelectric properties of halide perovskite $KGeI_{3-x}Br_x$ materials: photovoltaic applications. *Applied Physics A*, 127:1–7, 2021.

[5] Muhammad Iqbal Hussain, RM Arif Khalil, Fayyaz Hussain, A Manzoor Rana, G Murtaza, and M Imran. Probing the structural, electronic, mechanical strength and optical properties of tantalum-based oxide perovskites $ATaO_3$ (A = Rb, Fr) for optoelectronic applications: First-principles investigations. *Optik*, 219:165027, 2020.

[6] Muhammad Iqbal Hussain, RM Arif Khalil, Fayyaz Hussain, Muhammad Imran, Anwar Manzoor Rana, and Sungjun Kim. Investigations of structural,

electronic and optical properties of $YInO_3$ (Y= Rb, Cs, Fr) perovskite oxides using mBJ approximation for optoelectronic applications: a first principles study. *Materials Science in Semiconductor Processing*, 113:105064, 2020.

[7] G Murtaza, Iftikhar Ahmad, B Amin, A Afaq, M Maqbool, J Maqssod, I Khan, and M Zahid. Investigation of structural and optoelectronic properties of $BaThO_3$. *Optical Materials*, 33(3):553–557, 2011.

[8] NA Noor, Q Mahmood, M Rashid, Bakhtiar Ul Haq, and A Laref. The pressure-induced mechanical and optoelectronic behavior of cubic perovskite $PbSnO_3$ via ab-initio investigations. *Ceramics International*, 44(12):13750–13756, 2018.

[9] Md Rasidul Islam, Biazid Kabir Moghal, and Raza Moshwan. Tuning the electronic, optical, and thermal properties of cubic perovskites $CsPbCl_{3-n}Br_n$ ($n =$ 0, 1, 2, and 3) through altering the halide ratio. *Physica Scripta*, 97(6):065704, 2022.

[10] Yongbo Yuan, Jungseok Chae, Yuchuan Shao, Qi Wang, Zhengguo Xiao, Andrea Centrone, and Jinsong Huang. Photovoltaic switching mechanism in lateral structure hybrid perovskite solar cells. *Advanced Energy Materials*, 5(15), 2015.

[11] Samuel D Stranks, Giles E Eperon, Giulia Grancini, Christopher Menelaou, Marcelo JP Alcocer, Tomas Leijtens, Laura M Herz, Annamaria Petrozza, and Henry J Snaith. Electron-hole diffusion lengths exceeding 1 micrometer in an organometal trihalide perovskite absorber. *Science*, 342(6156):341–344, 2013.

[12] Qi-Jun Liu, Zheng-Tang Liu, Li-Ping Feng, and Hao Tian. Study of structural, elastic, electronic and optical properties of seven $SrZrO_3$ phases: First-principles calculations. *Journal of Solid State Chemistry*, 196:425–434, 2012.

[13] SSA Gillani, Riaz Ahmad, Muhammad Rizwan, Muhammad Rafique, Ghulam Ullah, CB Cao, and HB Jin. Effect of magnesium doping on band gap and optical properties of $SrZrO_3$ perovskite: a first-principles study. *Optik*, 191:132–138, 2019.

[14] JA Souza and JP Rino. A molecular dynamics study of structural and dynamical correlations of $CaTiO_3$. *Acta Materialia*, 59(4):1409–1423, 2011.

[15] Pornsawan Sikam, Pairot Moontragoon, Chayanin Sararat, Attaphol Karaphun, Ekaphan Swatsitang, Supree Pinitsoontorn, and Prasit Thongbai. DFT calculation and experimental study on structural, optical and magnetic properties of Co-doped $SrTiO_3$. *Applied Surface Science*, 446:92–113, 2018.

[16] Mahpara Ghazanfar, Sikander Azam, Muhammad Farooq Nasir, Souraya Goumri-Said, and Hussein Alrobei. Insight into electronic and optical properties of Eu+ 2-doped $CaTiO_3$ from GGA+ U calculations. *Journal of Solid State Chemistry*, 293:121796, 2021.

[17] O Lobacheva, YM Yiu, N Chen, TK Sham, and LV Goncharova. Changes in local surface structure and Sr depletion in Fe-implanted $SrTiO_3$ (001). *Applied Surface Science*, 393:74–81, 2017.

[18] Simone Sanna, Christian Thierfelder, S Wippermann, Tripurari Prasad Sinha, and Wolf Gero Schmidt. Barium titanate ground-and excited-state properties from first-principles calculations. *Physical Review B—Condensed Matter and Materials Physics*, 83(5):054112, 2011.

[19] Naveed Ahmed Noor, M Rashid, Qasim Mahmood, B Ul Haq, MA Naeem, and Amel Laref. Optoelectronic pressure dependent study of $MgZrO_3$ oxide and ground state thermoelectric response using Ab-initio calculations. *Opto-Electronics Review*, 27(2):194–201, 2019.

[20] DM Hoat, JF Rivas Silva, and A Méndez Blas. First principles study of structural, electronic and optical properties of perovskites $CaZrO_3$ and $CaHfO_3$ in cubic phase. *Solid State Communications*, 275:29–34, 2018.

[21] ZF Hou. Ab initio calculations of elastic modulus and electronic structures of cubic $CaZrO_3$. *Physica B: Condensed Matter*, 403(17):2624–2628, 2008.

[22] Md Atikur Rahman, Wakil Hasan, Rukaia Khatun, Md Zahid Hasan, Md Hafijur Rahman, Sushmita Sarker, Mahbub Hasan, and Jannatul Ferdous Lubna. An ab-initio study to investigate the structural, mechanical, electrical, optical and thermal properties of the $AZrO_3$ (A = Mg, Ca, Sr, Ba, Sn, Cu) compounds. *Materials Today Communications*, 34:105339, 2023.

[23] Muhammad Rashid, RB Behram, Farooq Aziz, Asif Mahmood, Nessrin A Kattan, and SM Ramay. Optoelectronic pressure dependent study of alkaline

earth based zirconates $AZrO_3$ (A = Ca, Ba, Sr) using ab-initio calculations. *The European Physical Journal B*, 93:1–9, 2020.

[24] I Zeba, M Ramzan, Riaz Ahmad, M Shakil, M Rizwan, M Rafique, M Sarfraz, M Ajmal, and SSA Gillani. First-principles computation of magnesium doped $CaZrO_3$ perovskite: a study of phase transformation, bandgap engineering and optical response for optoelectronic applications. *Solid State Communications*, 313:113907, 2020.

[25] Yu-Liang Liu, Chuan-Lu Yang, Mei-Shan Wang, Xiao-Guang Ma, and You-Gen Yi. Te-doped perovskite $NaTaO_3$ as a promising photocatalytic material for hydrogen production from water splitting driven by visible light. *Materials Research Bulletin*, 107:125–131, 2018.

[26] I Ait Brahim, N Bekkioui, M Tahiri, and H Ez-Zahraouy. Doping effect of chalcogens on electronic and optical properties of perovskite $LiNbO_3$ compound: Ab initio calculations. *Chemical Physics*, 550:111320, 2021.

[27] Zhonghai Yu, Chenhua Deng, Sen Kong, Haolei Hui, Jiale Guo, Qizhong Zhao, Fanghua Tian, Chao Zhou, Yin Zhang, Sen Yang, et al. Transition metal-doped chalcogenide perovskite magnetic semiconductor $BaZrS_3$. *Journal of Magnetism and Magnetic Materials*, 563:169886, 2022.

[28] B Akenoun, S Dahbi, N Tahiri, O El Bounagui, H Ez-Zahraouy, and A Benyoussef. The effect of chalcogens-doped with dilation strain on the electronic, optic, and thermoelectric properties of perovskite $BaSnO_3$ compound. *Journal of the Korean Ceramic Society*, 59(5):715–728, 2022.

[29] H Akter, MM Hossain, MM Uddin, SH Naqib, and MA Ali. Effects of S substitution on the structural, optoelectronic, and thermomechanical properties of $KTaO_3$ through density functional theory. *Journal of Physics and Chemistry of Solids*, 190:112021, 2024.

[30] RM Arif Khalil, Muhammad Iqbal Hussain, Rabail Fatima, Fayyaz Hussain, Anwar Manzoor Rana, HH Hegazy, and Abeer Mera. Effect of dopants on the structural, optoelectronic and magnetic properties of pristine $AgGaO_3$ perovskite: A first principles study. *Optik*, 244:167555, 2021.

[31] H Labrim, Y Selmani, S Ziti, S Idrissi, R El Bouayadi, D Zejli, and L Bahmad. Study of the perovskites $CaZrO_{3-x}S_x$ (x = 0, 1, 2 and 3) for photovoltaic applications. *Solid State Communications*, 363:115105, 2023.

[32] B Mouhib, S Dahbi, A Douayar, N Tahiri, O El Bounagui, and H Ez-Zahraouy. Theoretical investigations of electronic structure and optical properties of S, Se or Te doped perovskite $ATiO_3$ (A = Ca, Ba, and Sr) materials for eco-friendly solar cells. *Micro and Nanostructures*, 163:107124, 2022.

[33] S Dahbi, N Tahiri, O El Bounagui, and H Ez-Zahraouy. The new eco-friendly lead-free zirconate perovskites doped with chalcogens for solar cells: Ab initio calculations. *Optical Materials*, 109:110442, 2020.

[34] H Zitouni, N Tahiri, O El Bounagui, and H Ez-Zahraouy. Electronic, optical and transport properties of perovskite $BaZrS_3$ compound doped with Se for photovoltaic applications. *Chemical Physics*, 538:110923, 2020.

[35] Robert G Parr and Weitao Yang. Density-functional theory of the electronic structure of molecules. *Annual Review of Physical Chemistry*, 46(1):701–728, 1995.

[36] David J Griffiths and Darrell F Schroeter. Introduction to quantum mechanics. 2018.

[37] Erwin Schrödinger. An undulatory theory of the mechanics of atoms and molecules. *Physical Review*, 28(6):1049, 1926.

[38] Paul Adrien Maurice Dirac. The physical interpretation of the quantum dynamics. *Proceedings of the Royal Society of London. Series A, Containing Papers of a Mathematical and Physical Character*, 113(765):621–641, 1927.

[39] David C Young. Density functional theory. *Computational Chemistry*, pages 42–48, 2001.

[40] Wolfgang Pauli. The connection between spin and statistics. *Physical Review*, 58(8):716, 1940.

[41] Arthur Jabs. Connecting spin and statistics in quantum mechanics. *Foundations of Physics*, 40:776–792, 2010.

[42] Attila Szabo and Neil S Ostlund. *Modern quantum chemistry: introduction to advanced electronic structure theory*. Courier Corporation, 2012.

[43] Nouredine Zettili. Quantum mechanics: concepts and applications. 2009.

[44] Libero J Bartolotti and Ken Flurchick. An introduction to density functional theory. *Reviews in Computational Chemistry*, pages 187–216, 1996.

[45] E BRoDA. Nuclear chemistry. *Chemistry Today: A Guide for Teachers: Selected Topics for a Modern Approach to the Teaching of School Chemistry*, page 3355, 1963.

[46] Niklas Zwettler. Density functional theory.

[47] Jan Almlöf. Notes on Hartree-Fock theory and related topics. *Lecture Notes in Quantum Chemistry II: European Summer School in Quantum Chemistry*, pages 1–90, 1994.

[48] Phillip James Edwin Peebles. *Quantum mechanics*. Princeton University Press, 1992.

[49] Albert T Fromhold. *Quantum mechanics for applied physics and engineering*. Courier Corporation, 2012.

[50] P Lykos and GW Pratt. Discussion on the Hartree-Fock approximation. *Reviews of Modern Physics*, 35(3):496, 1963.

[51] Charlotte Froese Fischer. Hartree Fock method for atoms. A numerical approach. 1977.

[52] Wolfram Koch and Max C Holthausen. *A chemist's guide to density functional theory*. John Wiley & Sons, 2015.

[53] Robert G Parr. Density functional theory. *Electron Distributions and the Chemical Bond*, pages 95–100, 1982.

[54] Walter Kohn. Electronic structure of matter-wave functions and density functionals. *Rev. Mod. Phys.*, 71(5):1253–1266, 1999.

[55] Per-Olov Löwdin. Scaling problem, virial theorem, and connected relations in quantum mechanics. *Journal of Molecular Spectroscopy*, 3(1-6):46–66, 1959.

[56] Pierre Hohenberg and Walter Kohn. Inhomogeneous electron gas. *Physical Review*, 136(3B):B864, 1964.

[57] Stig Lundqvist and Norman H March. *Theory of the inhomogeneous electron gas*. Springer Science & Business Media, 2013.

[58] JMC Scott. LXXXII. The binding energy of the Thomas-Fermi Atom. *The London, Edinburgh, and Dublin Philosophical Magazine and Journal of Science*, 43(343):859–867, 1952.

[59] Klaus Capelle. A bird's-eye view of density-functional theory. *Brazilian Journal of Physics*, 36:1318–1343, 2006.

[60] Philip Peter Rushton. *Towards a non-local density functiona description of exchange and correlation*. PhD thesis, Durham University, 2002.

[61] Elliot H Lieb. Variational principle for many-fermion systems. *Physical Review Letters*, 46(7):457, 1981.

[62] Stefaan Cottenier et al. Density Functional Theory and the family of LAPW-methods: a step-by-step introduction. *Instituut voor Kern-en Stralingsfysica, KU Leuven, Belgium*, 4(0):41, 2002.

[63] Walter Kohn and Lu Jeu Sham. Self-consistent equations including exchange and correlation effects. *Physical Review*, 140(4A):A1133, 1965.

[64] Richard M Martin. *Electronic structure: basic theory and practical methods*. Cambridge university press, 2020.

[65] Pawel Scharoch and Maciej Winiarski. An efficient method of DFT/LDA band-gap correction. *Computer Physics Communications*, 184(12):2680–2683, 2013.

[66] Axel D Becke. Density-functional exchange-energy approximation with correct asymptotic behavior. *Physical Review A*, 38(6):3098, 1988.

[67] Ulf Von Barth and Lars Hedin. A local exchange-correlation potential for the spin polarized case. i. *Journal of Physics C: Solid State Physics*, 5(13):1629, 1972.

[68] Gang Zhang and Charles B Musgrave. Comparison of DFT methods for molecular orbital eigenvalue calculations. *The Journal of Physical Phemistry A*, 111(8):1554–1561, 2007.

[69] Matteo Cococcioni and Stefano De Gironcoli. Linear response approach to the calculation of the effective interaction parameters in the LDA+ U method. *Physical Review B—Condensed Matter and Materials Physics*, 71(3):035105, 2005.

[70] Walter Kohn. Nobel lecture: Electronic structure of matter-wave functions and density functionals. *Reviews of Modern Physics*, 71(5):1253, 1999.

[71] P. Blaha, K. Schwarz, P. Sorantin, and S.B. Trickey. Full-potential, linearized augmented plane wave programs for crystalline systems. *Computer Physics Communications*, 59(2):399–415, 1990.

[72] Georg K. H. Madsen, Peter Blaha, Karlheinz Schwarz, Elisabeth Sjöstedt, and Lars Nordström. Efficient linearization of the augmented plane-wave method. *Phys. Rev. B*, 64:195134, Oct 2001.

[73] Peter Blaha, Karlheinz Schwarz, Georg Madsen, D. Kvasnicka, and J. Luitz. WIEN2k: An augmented plane wave plus local orbitals program for calculating crystal properties. *Technische Universität Wien, Wien*, 28, 01 2001.

[74] P. Hohenberg and W. Kohn. Inhomogeneous electron gas. *Phys. Rev.*, 136:B864–B871, Nov 1964.

[75] M. Städele, J. A. Majewski, P. Vogl, and A. Görling. Exact Kohn-Sham exchange potential in semiconductors. *Phys. Rev. Lett.*, 79:2089–2092, Sep 1997.

[76] P. Blaha, K. Schwarz, P. Sorantin, and S.B. Trickey. Full-potential, linearized augmented plane wave programs for crystalline systems. *Computer Physics Communications*, 59(2):399–415, 1990.

[77] Zhimei Sun, Sa Li, Rajeev Ahuja, and Jochen M. Schneider. Calculated elastic properties of M_2AlC (M = Ti, V, Cr, Nb and Ta). *Solid State Communications*, 129(9):589–592, 2004.

[78] Akeem Adekunle Adewale, Abdullah Chik, Tijjani Adam, Olaniyi Kamil Yusuff, Sabur Abiodun Ayinde, and Yekinni Kolawole Sanusi. First principles calculations of structural, electronic, mechanical and thermoelectric properties of cubic $ATiO_3$ (A= Be, Mg, Ca, Sr and Ba) perovskite oxide. *Computational Condensed Matter*, 28:e00562, 2021.

[79] Sadia Riaz, Muhammad Yaseen, Mehwish Khalid Butt, Shanza Mubashir, Javed Iqbal, Abeer S. Altowyan, A. Dahshan, Adil Murtaza, Munawar Iqbal, and A. Laref. Physical characteristics of $NaTaO_3$ under pressure for electronic devices. *Materials Science in Semiconductor Processing*, 133:105976, 2021.

[80] Narasak Pandech, Kanoknan Sarasamak, and Sukit Limpijumnong. Elastic properties of perovskite $ATiO_3$ (A = Be, Mg, Ca, Sr, and Ba) and $PbBO_3$ (B = Ti, Zr, and Hf): first principles calculations. *Journal of Applied Physics*, 117(17), 2015.

[81] F Chiker, B Abbar, B Bouhafs, and P Ruterana. Interband transitions of wide-band-gap ternary pnictide $BeCN_2$ in the chalcopyrite structure. *Physica Ptatus Solidi (b)*, 241(2):305–316, 2004.

[82] A Hossain, MA Ali, MM Uddin, SH Naqib, and MM Hossain. Theoretical studies on phase stability, electronic, optical, mechanical and thermal properties of chalcopyrite semiconductors $HgXN_2$ (X= Si, Ge and Sn): a comprehensive DFT analysis. *Materials Science in Semiconductor Processing*, 172:108092, 2024.

[83] H. Absike, N. Baaalla, L. Attou, H. Labrim, B. Hartiti, and H. Ez-zahraouy. Theoretical investigations of structural, electronic, optical and thermoelectric properties of oxide halide perovskite $ACoO_3$ (A = Nd, Pr or La). *Solid State Communications*, 345:114684, 2022.

[84] S. Parida, S.K. Rout, L.S. Cavalcante, E. Sinha, M. Siu Li, V. Subramanian, N. Gupta, V.R. Gupta, J.A. Varela, and E. Longo. Structural refinement, optical and microwave dielectric properties of $BaZrO_3$. *Ceramics International*, 38(3):2129–2138, 2012.

[85] G. Murtaza, N. Yousaf, A. Laref, and M. Yaseen. Effect of varying pnictogen elements (Pn = N, P, As, Sb, Bi) on the optoelectronic properties of $SrZn_2Pn_2$. *Zeitschrift für Naturforschung A*, 73(4):285–293, 2018.

[86] Md Atikur Rahman, Mahbub Hasan, Jannatul Ferdous Lubna, Rukaia Khatun, Sushmita Sarker, Md Zahid Hasan, Aslam Hossain, Md Mukter Hossain, Md Rasheduzzaman, Wakil Hasan, et al. Comparative study of the structural, mechanical, electronic, optical and thermodynamic properties of superconducting disilicide YT_2Si_2 (T= Co, Ni, Ru, Rh, Pd, Ir) by DFT simulation. *Journal of Physics and Chemistry of Solids*, 178:111342, 2023.

[87] Jay N Zemel, James D Jensen, and Richard B Schoolar. Electrical and optical properties of epitaxial films of PbS, PbSe, PbTe, and SnTe. *Physical Review*, 140(1A):A330, 1965.

[88] Max Born. On the stability of crystal lattices. I. 36(2):160–172, 1940.

[89] Ibrahim Isah, Salisu I Kunya, Sani Abdulkarim, and Bello Usama Ibrahim. Effect of pressure on structural, elastic and electronic properties of perovskite $PbTiO_3$. *Journal for Foundations and Applications of Physics*, 8(2):179–190, 2021.

[90] Richard Hill. The elastic behaviour of a crystalline aggregate. *Proceedings of the Physical Society. Section A*, 65(5):349, 1952.

[91] Saad Tariq, Afaq A, Saher Saad, and Samar Tariq. Structural, electronic and elastic properties of the cubic $CaTiO_3$ under pressure: A DFT study. *AIP Advances*, 5, 07 2015.

[92] M. Mozahar Ali, M.A. Hadi, Istiak Ahmed, A.F.M.Y. Haider, and A.K.M.A Islam. Physical properties of a novel boron-based ternary compound Ti_2InB_2. *Materials Today Communications*, 25:101600, 2020.

[93] WANG Yunjie, ZHANG Zhiyuan, WEN Dulin, WU Zhencheng, and SU Xin. First principles study on mechanical properties, electronic structure and optical properties of Ni, Cu, Zn doped tetragonal $PbTiO_3$. *Journal of Synthetic Crystals*, 53(2), 2024.

[94] M.A. Ali and Muhammad Waqas Qureshi. DFT insights into the new Hf-based chalcogenide MAX phase Hf_2SeC. *Vacuum*, 201:111072, 2022.

[95] Mauwa M Namisi, Robinson J Musembi, Winfred M Mulwa, and Bernard O Aduda. DFT study of cubic, tetragonal and trigonal structures of $KGeCl_3$ perovskites for photovoltaic applications. *Computational Condensed Matter*, 34:e00772, 2023.

[96] Mumtaz Manzoor, Debidatta Behera, Ramesh Sharma, Muhammad Waqas Iqbal, Sanat Kumar Mukherjee, Rabah Khenata, Saleh S Alarfaji, and Huda A Alzahrani. Investigation of the structural, mechanical, optoelectronic and, thermoelectric characteristics of cubic $GeTiO_3$: An ab initio study. *Materials Today Communications*, 34:105053, 2023.

[97] Nadjia Tayebi, Kada Bidai, Mohammed Ameri, Slamani Amel, Ibrahim Ameri, Y Al-Douri, and Dinesh Varshney. Pressure and temperature dependence of the structural, elastic and thermodynamic properties of potassium telluride: First-principles calculations. *Chinese Journal of Physics*, 55(3):769–779, 2017.

[98] Amel Hachemi, H Hachemi, A Ferhat-Hamida, and Layachi Louail. Elasticity of $SrTiO_3$ perovskite under high pressure in cubic, tetragonal and orthorhombic phases. *Physica Scripta*, 82(2):025602, 2010.

[99] Xiong Yang, Ying Wang, Qinggong Song, Yifei Chen, and Yan Hong Xue. Pressure effects on structural, electronic, elastic, and optical properties of cubic and tetragonal phases of $BaZrO_3$. *Acta Physica Polonica A*, 133(5):1138–1143, 2018.

[100] Li Li, Donald J Weidner, John Brodholt, Dario Alfe, G David Price, Razvan Caracas, and Renata Wentzcovitch. Elasticity of $CaSiO_3$ perovskite at high pressure and high temperature. *Physics of the Earth and Planetary Interiors*, 155(3-4):249–259, 2006.

[101] Orson L Anderson. A simplified method for calculating the debye temperature from elastic constants. *Journal of Physics and Chemistry of Solids*, 24(7):909–917, 1963.

[102] Sajad Ahmad Dar, Ramesh Sharma, and Abhishek Kr Mishra. Phonon stability, electronic structure results, mechanical and thermodynamic properties of $RbSbO_3$ and $CsSbO_3$ perovskite oxides: Ab initio investigation. *Journal of Molecular Graphics and Modelling*, 90:120–127, 2019.

[103] Zi-jiang Liu, Xiao-wei Sun, Cai-rong Zhang, Jian-bo Hu, Ting Song, and Jian-hong Qi. Elastic tensor and thermodynamic property of magnesium silicate perovskite from first-principles calculations. *Chinese Journal of Chemical Physics*, 24(6):703, 2011.

[104] MA Ali, N Jahan, and AKMA Islam. Sulvanite compounds Cu_3TMS_4 (TM = V, Nb and Ta): elastic, electronic, optical and thermal properties using first-principles method. *arXiv preprint arXiv:1510.05564*, 2015.

[105] Jianping Long, Lijun Yang, and Xuesong Wei. Lattice, elastic properties and debye temperatures of $ATiO_3$ (A = Ba, Ca, Pb, Sr) from first-principles. *Journal of Alloys and Compounds*, 549:336–340, 2013.

[106] A Boudali, M Driss Khodja, B Amrani, D Bourbie, K Amara, and A Abada. First-principles study of structural, elastic, electronic, and thermal properties of $SrTiO_3$ perovskite cubic. *Physics Letters A*, 373(8-9):879–884, 2009.

[107] Akira Yoshiasa, Tomotaka Nakatani, Akihiko Nakatsuka, Maki Okube, Kazumasa Sugiyama, and Tsutomu Mashimo. High-temperature single-crystal X-ray diffraction study of tetragonal and cubic perovskite-type $PbTiO_3$ phases. *Acta Crystallographica Section B: Structural Science, Crystal Engineering and Materials*, 72(3):381–388, 2016.